AIAA SciTech Forum
7-11 January 2019, San Diego, California
AIAA Scitech 2019 Forum

10.2514/6.2019-2227

AIAA SciTech Conference, 7–11 Jan 2019, San Diego, CA

Hybrid Shell Model for Aeroelastic Modeling

Mark Drela*, Marshall Galbraith†, Steven Allmaras‡
Massachusetts Institute of Technology, Cambridge, MA 02139, U.S.A.

The paper presents the HSM finite element formulation which extends common existing C^0-continuous large-deflection shell methods by the introduction of spherical interpolation of unit basis vectors, and higher-order representations of a virtual C^1 continuous shell surface and its covariant basis vectors. These modifications greatly improve accuracy for elements which are highly curved, either in the undeformed case or after deformation, with the result that HSM can tolerate very coarse grids, especially in bending-dominated problems. This makes the method particularly well suited for intermediate-fidelity aeroelastic modeling, since coarse surface grids on aerodynamic bodies naturally results in highly-curved elements. Various structural phenomena common in nonlinear aeroelasticity, such as large deformations and buckling, can be thus be predicted with modest cost.

Nomenclature

$\boldsymbol{a}$	acceleration
$\mathbf{a}_\alpha, \mathbf{a}^\alpha$	covariant and contravariant basis vectors
$\mathbf{b}$	residual projection vector
$\hat{\mathbf{c}}_1, \hat{\mathbf{c}}_2$	element in-surface cartesian basis vectors
$\hat{\mathbf{d}}$	material quasi-normal vector (director)
$\hat{\mathbf{e}}_1, \hat{\mathbf{e}}_2$	nodal in-surface cartesian basis vectors
$\bar{\bar{\mathbf{f}}}$	shell stress resultant tensor
$\mathbf{g}$	acceleration of gravity
$\breve{g}_{\alpha\beta}$	metric tensor components
$\breve{h}_{\alpha\beta}$	curvature tensor components
$\breve{\ell}_\alpha$	director lean vector components
$\hat{\mathbf{l}}$	shell perimeter unit vector
J	element-coordinate Jacobian
$\bar{\bar{\mathbf{m}}}$	shell stress-moment resultant tensor
$\hat{\mathbf{n}}$	shell normal unit vector
N_i	element interpolation basis function
$\mathbf{q}$	shell force loading vector
$\mathbf{r}$	position vector
$\mathcal{R}$	residual
$\hat{\mathbf{t}}$	shell-tangential edge normal unit vector
t	time
$\mathbf{U}$	frame velocity
W_i	residual weighting function
α, β	element-basis indices, 1 or 2
$\boldsymbol{\gamma}$	transverse shear strain vector
$\bar{\bar{\boldsymbol{\varepsilon}}}$	in-surface strain tensor
$\bar{\bar{\boldsymbol{\sigma}}}$	stress tensor
ξ, η	element coordinates
$\boldsymbol{\lambda}$	log-quaternion
ρ	volume mass density
μ	area mass density
ς	first-moment area mass density
$\boldsymbol{\tau}$	shell moment-loading vector
$\boldsymbol{\Omega}$	frame rotation rate

Subscripts and Superscripts

$()_i$	quantity at node i
$()_n$	shell-normal component
$()_0$	undeformed-state quantity
$()_{a,b}$	components in element cartesian $\hat{\mathbf{c}}_1, \hat{\mathbf{c}}_2$ basis
$()_{i,j}$	components in nodal cartesian $\hat{\mathbf{e}}_1, \hat{\mathbf{e}}_2$ basis
$\breve{()}_\alpha$	covariant components in element $\mathbf{a}_\alpha$ basis
$\breve{()}^\alpha$	contravariant components in element $\mathbf{a}^\alpha$ basis
$\widetilde{\nabla}()$	tangential gradient (excludes $\hat{\mathbf{n}}$ component)

*Terry J. Kohler Professor, AIAA Fellow
†Research Engineer, AIAA Member
‡Research Engineer, AIAA Associate Fellow

I. Introduction

The Fluid-Structure Interaction (FSI) problem has been the topic of extensive research. It can be implemented in several levels of fidelity, from full nonlinear treatment where the (possibly large) structural deformation modifies both the structure and fluid-domain geometries, to linearized formulations where all deformation perturbations are assumed small. The present treatment is aimed at intermediate-fidelity FSI solutions, using a structural shell model allowing possibly large deformations. One advantage of a shell model is that it can approximate the behavior of a relatively complex structure with stringers, doublers, etc. by lumping these details into a monolithic shell with the equivalent mass and stiffnesses. This monolithic shell requires many fewer parameters to describe, and is therefore better suited for early design and optimization, or if the structure is driven by and coupled with an aerodynamic solver. The lumping procedure can of course be carried further by representing the structure as a beam. This then gives a very simple structural problem, but it causes modeling uncertainties for low to moderate aspect ratios, and also at body intersections in general. Since a shell model can be formulated on the actual body outer mold line (OML) surface, these beam-modeling difficulties are largely circumvented.

The earliest numerical solutions of shell problems with general geometry, such as the pioneering work of Ahmad, Irons, and Zienkewicz,[1] treated the shell elements as degenerate 3D solids. These circumvented the complexity of global curvilinear coordinates[2] by formulating the problem in 3D cartesian space, with the node position vectors $\mathbf{r}$ and material quasi-normal vectors (or director) $\hat{\mathbf{d}}$ as the primary unknowns. However, the early formulations suffered from shear locking, where the representation of the transverse shear strains via the interpolated element $\mathbf{r}$ and $\hat{\mathbf{d}}$ fields was inconsistent in the thin-shell limit.

More recent shell model developments, such as those of of Dvorkin and Bathe,[3] sidestep the shear locking problem via the MITC scheme, where the transverse shear strain field is defined by a special interpolation scheme from the edge midpoints (not nodes) of a quadrilateral element. Simo et al,[45] further refined this model, and Lee, Lee, and Bathe[6] extended the approach to triangular elements. Talamini[7] developed a Discontinuous-Galerkin version applicable to both quad or triangular elements.

The present Hybrid Shell Model (HSM) starts with the basic bilinear MITC formulation, but introduces spherical (quaternion) interpolation for the director field, and also for the local cartesian basis vectors used to interpolate specified nodal stiffness tensors and loads. The element covariant basis vectors and the moment arm appearing in the angular momentum equation are also modified to exploit the higher-order geometry information contained in the director field, so that the governing equations are in effect formulated on a virtual C^1-continuous surface, rather than the standard C^0 surface of conventional bilinear finite element treatments. The result is a large improvement in accuracy with highly-curved elements and bending-dominated problems. The method's performance is demonstrated with a few representative test cases and also with realistic aeroelastic problems.

II. Geometry

As shown in Figure 1, the geometry of the undeformed shell's reference surface is specified by the $\mathbf{r}_{0(\xi,\eta)}$ position vector, which also has a unit normal $\hat{\mathbf{n}}_{0(\xi,\eta)}$, both being functions of the surface material coordinates ξ, η. Non-isotropic shell materials also require choosing tangent vectors $\hat{\mathbf{e}}_{0_1}, \hat{\mathbf{e}}_{0_2}$ which define the basis in which the shell stiffness tensors are specified.

The deformed shell geometry is defined by the position vector $\mathbf{r}_{(\xi,\eta)}$ of the shell reference surface and the material quasi-normal vector (or director) $\hat{\mathbf{d}}_{(\xi,\eta)}$. Following standard formulations,[1,3,4] the position $\mathbf{r}'$ of an arbitrary material point off the reference surface is then given by

$$\mathbf{r}'_{(\xi,\eta,\zeta)} \;=\; \mathbf{r} \,+\, \zeta\,\hat{\mathbf{d}} \tag{1}$$

where ζ is the distance from the reference surface along $\hat{\mathbf{d}}$. The normal vector is related to the director by

$$\hat{\mathbf{n}}_{(\xi,\eta)} \;=\; \frac{\hat{\mathbf{d}} - \boldsymbol{\ell}}{|\hat{\mathbf{d}} - \boldsymbol{\ell}|} \;\simeq\; \hat{\mathbf{d}} \,-\, \boldsymbol{\ell} \tag{2}$$

where $\boldsymbol{\ell}_{(\xi,\eta)}$ is the director lean vector, shown in Figure 2. This is assumed to be small and perpendicular to $\hat{\mathbf{n}}$, so that the approximation in (2) is valid to first order, and ζ is also the normal coordinate n to first

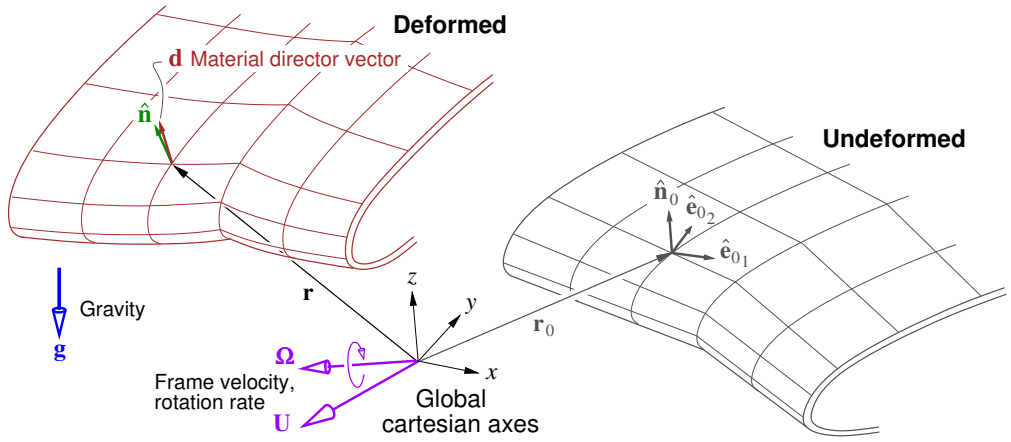

Figure 1. Shell geometry defined by deformed and undeformed position vectors $\mathbf{r}, \mathbf{r}_0$. Anisotropic shell properties are defined along local $\hat{\mathbf{e}}_{0_1}, \hat{\mathbf{e}}_{0_2}, \hat{\mathbf{n}}_0$ basis vectors. Frame velocity $\mathbf{U}(t)$ and rotation rate $\boldsymbol{\Omega}(t)$ relative to some other inertial frame are used in dynamic problems. All vectors are defined via components along global xyz axes.

order. For the undeformed geometry which by definition has zero strain, it is convenient to choose $\hat{\mathbf{d}}_0 = \hat{\mathbf{n}}_0$, so that $\boldsymbol{\ell}_0 = \mathbf{0}$ and $\zeta = n$ exactly. With these choices the lean vector is also the transverse shear strain vector, $\boldsymbol{\gamma} \equiv \boldsymbol{\ell} - \boldsymbol{\ell}_0 = \boldsymbol{\ell}$, which will be assumed from now on.

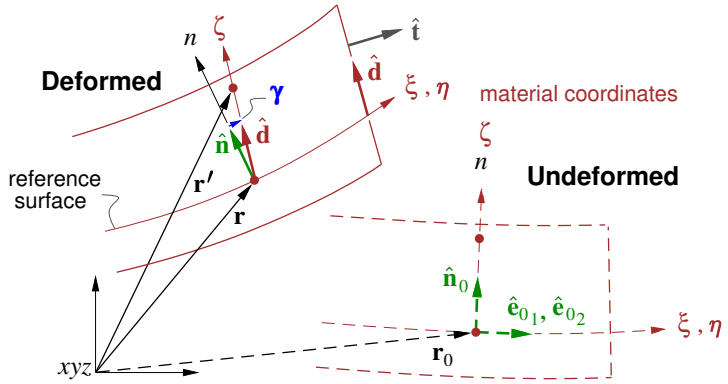

Figure 2. View through thickness of shell showing material-point position $\mathbf{r}'$, reference-surface position $\mathbf{r}$, and material director $\hat{\mathbf{d}}$. Edge boundary conditions are defined using edge unit normal vector $\hat{\mathbf{t}}$. Stiffness tensors are defined along the arbitrary in-surface basis vectors $\hat{\mathbf{e}}_{0_1}, \hat{\mathbf{e}}_{0_2}$.

III. Stress Resultant Integrals

A. Resultant Definitions

The integral momentum and angular-momentum equations for a shell will involve the following mass, mass-moment, stress, and stress-moment resultant integrals over the shell thickness, which are then functions of the surface coordinates ξ, η.

$$\mu(\xi,\eta) \equiv \int_{\zeta_{\text{bot}}}^{\zeta_{\text{top}}} \rho \, \mathrm{d}\zeta \quad , \qquad \varsigma(\xi,\eta) \equiv \int_{\zeta_{\text{bot}}}^{\zeta_{\text{top}}} \rho\,\zeta \, \mathrm{d}\zeta \tag{3}$$

$$\bar{\bar{\mathbf{f}}}(\xi,\eta) \equiv \int_{\zeta_{\text{bot}}}^{\zeta_{\text{top}}} \bar{\bar{\boldsymbol{\sigma}}} \, \mathrm{d}\zeta \quad , \qquad \bar{\bar{\mathbf{m}}}(\xi,\eta) \equiv \int_{\zeta_{\text{bot}}}^{\zeta_{\text{top}}} \bar{\bar{\boldsymbol{\sigma}}}\,\zeta \, \mathrm{d}\zeta \tag{4}$$

Coordinate Jacobians, which appear in the geometrically-exact formulation of Simo et al,[4] have been dropped from the integrands here since they reduce to unity in the limit of small shell thickness relative to its radius

of curvature, and also a small transverse shear strain, $|\gamma| \ll 1$. Note that this does not put any restrictions on the *element size* relative to the radius of curvature.

The bending moment/length tensor about the reference point $\zeta = 0$ is defined as $\hat{\mathbf{d}} \times \bar{\bar{\mathbf{m}}}$. At a shell element edge with unit edge-normal vector $\hat{\mathbf{t}}$ as shown in Figure 3, $\hat{\mathbf{d}} \times \bar{\bar{\mathbf{m}}} \cdot \hat{\mathbf{t}}$ is the edge bending moment/length vector, and $\bar{\bar{\mathbf{f}}} \cdot \hat{\mathbf{t}}$ is the overall edge traction force/length vector. Also appearing will be the net top–bottom surface traction stress and stress-moment.

$$\mathbf{q}(\xi,\eta) \;\equiv\; \bar{\bar{\boldsymbol{\sigma}}}_{\text{top}} \cdot \hat{\mathbf{n}}_{\text{top}} \;+\; \bar{\bar{\boldsymbol{\sigma}}}_{\text{bot}} \cdot \hat{\mathbf{n}}_{\text{bot}} \tag{5}$$

$$\boldsymbol{\tau}(\xi,\eta) \;\equiv\; \zeta_{\text{top}}\, \bar{\bar{\boldsymbol{\sigma}}}_{\text{top}} \cdot \hat{\mathbf{n}}_{\text{top}} \;+\; \zeta_{\text{bot}}\, \bar{\bar{\boldsymbol{\sigma}}}_{\text{bot}} \cdot \hat{\mathbf{n}}_{\text{bot}} \tag{6}$$

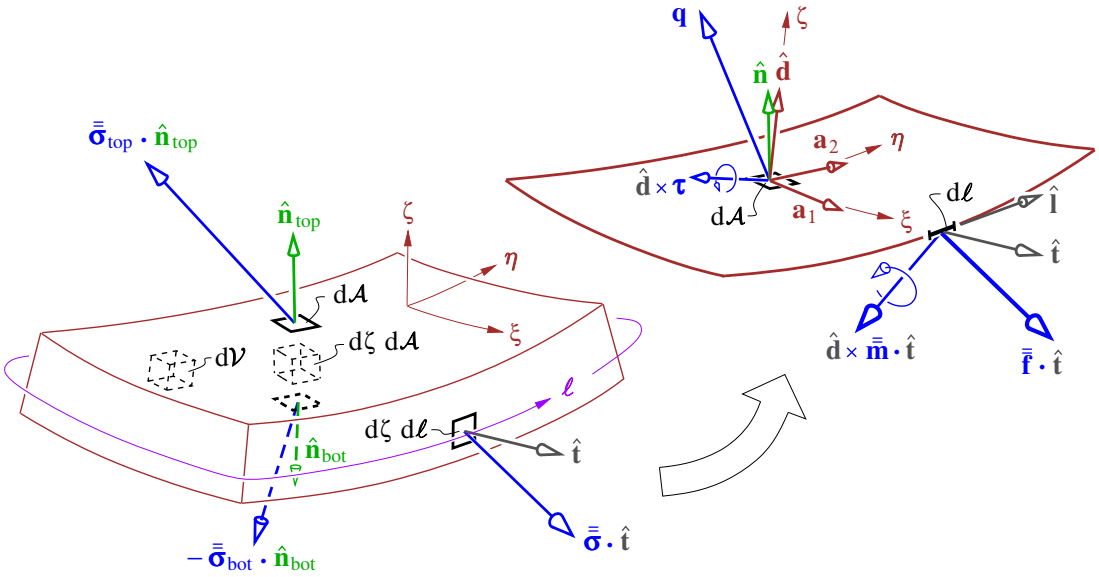

Figure 3. Shell element volume used to formulate integral momentum equations for the shell's lumped representation on the right. Tractions on volume surfaces become net force loading $\mathbf{q}$ on the shell area and force loading $\bar{\bar{\mathbf{f}}} \cdot \hat{\mathbf{t}}$ and moment loading $\hat{\mathbf{d}} \times \bar{\bar{\mathbf{m}}} \cdot \hat{\mathbf{t}}$ on the shell edges. The finite element implementation will be performed using local element coordinates ξ, η, and associated covariant basis vectors $\mathbf{a}_1, \mathbf{a}_2$.

B. Thin-Shell Approximations

In the thin-shell approximation the shell thickness h is assumed to be much smaller than a typical shell dimension L, as suggested by Figure 3.

$$\zeta_{\text{top}} - \zeta_{\text{bot}} \;\equiv\; h \;\ll\; L \tag{7}$$

In this case the torque of gravity and reference-surface acceleration acting on the mass-moment ς can be assumed to be negligible for a sufficiently thin shell.

$$\varsigma(\mathbf{g} - \boldsymbol{a}) \;\simeq\; \mathbf{0} \tag{8}$$

We will also assume that the shell thickness variations are small, $|\widetilde{\nabla} h| \ll 1$, so that the top and bottom surface normal vectors are nearly anti-parallel, i.e. $\hat{\mathbf{n}} = \hat{\mathbf{n}}_{\text{top}} = -\hat{\mathbf{n}}_{\text{bot}}$. The loading (5) can then be defined using only the reference-surface normal vector $\hat{\mathbf{n}}$, and the moment loading (6) is assumed negligible.

$$\mathbf{q}(\xi,\eta) \;\simeq\; (\bar{\bar{\boldsymbol{\sigma}}}_{\text{top}} - \bar{\bar{\boldsymbol{\sigma}}}_{\text{bot}}) \cdot \hat{\mathbf{n}} \tag{9}$$

$$\boldsymbol{\tau}(\xi,\eta) \;\simeq\; \mathbf{0} \tag{10}$$

These assumptions are made here only for simplicity, and all the dropped terms could be retained if desired.

IV. Discrete Shell Equations

The starting point for the discrete formulation is the 3D momentum and angular-momentum equations for a material with Cauchy stress tensor $\bar{\bar{\boldsymbol{\sigma}}}$, density ρ, acceleration $\boldsymbol{a}$, and gravity $\mathbf{g}$.

$$\nabla \cdot \bar{\bar{\boldsymbol{\sigma}}} \;+\; \rho\,(\mathbf{g}-\boldsymbol{a}) \;=\; \mathbf{0} \tag{11}$$

$$\nabla \cdot (\mathbf{r}'\times\bar{\bar{\boldsymbol{\sigma}}}) \;+\; \rho\,\mathbf{r}'\times(\mathbf{g}-\boldsymbol{a}) \;=\; \mathbf{0} \tag{12}$$

The standard shell analysis procedure is to reduce the volume momentum equations (11) and (12) to a shell manifold, and then discretize that with shell finite elements. Here we will go directly from the 3D equations to the discrete shell formulation via weighted-residual volume integration, using a weighting function whose variation through the shell thickness is diagrammed in Figure 4.

The discrete equations are obtained by multiplying (11) and (12) by the weighting function $W_{i(\xi,\eta)}$ which is nonzero only over the elements which contain node i, and whose isosurfaces lie along $\hat{\mathbf{d}}$, as diagrammed in Figure 4. We then combine W_i with the divergence terms and integrate over the shell volume.

$$\iiint \Big\{ \nabla \cdot (\bar{\bar{\boldsymbol{\sigma}}} W_i) \;-\; \bar{\bar{\boldsymbol{\sigma}}} \cdot \nabla W_i \;+\; \rho\,(\mathbf{g}-\boldsymbol{a})\,W_i \Big\}\, \mathrm{d}\mathcal{V} \;=\; \mathbf{0} \tag{13}$$

$$\iiint \Big\{ \nabla \cdot (\mathbf{r}'\times\bar{\bar{\boldsymbol{\sigma}}}\, W_i) \;-\; \mathbf{r}'\times\bar{\bar{\boldsymbol{\sigma}}} \cdot \nabla W_i \;+\; \rho\,\zeta\,\mathbf{r}'\times(\mathbf{g}-\boldsymbol{a})\,W_i \Big\}\, \mathrm{d}\mathcal{V} \;=\; \mathbf{0} \tag{14}$$

The first pure divergence terms are next replaced by area integrals over the perimeter surface with surface-tangent vector $\hat{\mathbf{t}}$ and area elements $\mathrm{d}\zeta\,\mathrm{d}\ell$, and over the top/bottom surfaces with normals $\pm\hat{\mathbf{n}}$ and area elements $\mathrm{d}\mathcal{A}$, all diagrammed in Figure 3. For the remaining terms, the volume element is written as $\mathrm{d}\mathcal{V} = \mathrm{d}\zeta\,\mathrm{d}\mathcal{A}$. We next introduce the tangential gradient which excludes any normal component along $\hat{\mathbf{n}}$,

$$\widetilde{\nabla} W_i \;\equiv\; \nabla W_i \;-\; (\hat{\mathbf{n}} \cdot \nabla W_i)\,\hat{\mathbf{n}} \tag{15}$$

as shown in Figure 4. We can then decompose the second stress terms in (13) and (14) as

$$\bar{\bar{\boldsymbol{\sigma}}} \cdot \nabla W \;=\; \bar{\bar{\boldsymbol{\sigma}}} \cdot \widetilde{\nabla} W \;+\; (\hat{\mathbf{n}} \cdot \nabla W_i)\,\bar{\bar{\boldsymbol{\sigma}}} \cdot \hat{\mathbf{n}} \tag{16}$$

and we note that the normal components will be very small for thin shells.

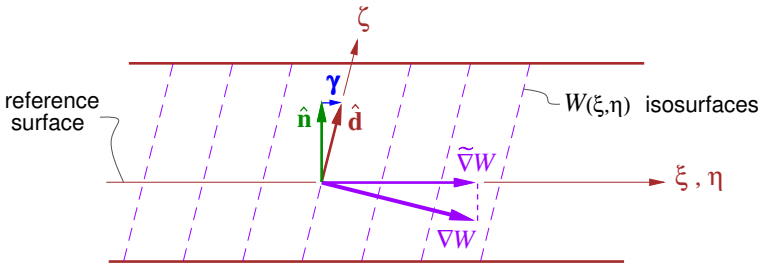

Figure 4. Weighting function gradient ∇W_i and tangential gradient $\widetilde{\nabla} W_i$, viewed through the shell thickness.

The integrations $\int \mathrm{d}\zeta$ across the shell thickness are now carried out, and the $\mathbf{q}$ and $\boldsymbol{\tau}$ definitions (9) are used for the top and bottom surface terms. The fact that $W_{i(\xi,\eta)}$ is defined to not vary in ζ enables it to be put outside the $\int \mathrm{d}\zeta$ thickness integrals, so that the μ, ς, $\bar{\bar{\mathbf{f}}}$, $\bar{\bar{\mathbf{m}}}$ definitions (4) and (4) can also be invoked. Equations (13) and (14) then become the linear and angular momentum residual vectors for node i.

$$\boldsymbol{\mathcal{R}}_i^f \;\equiv\; \oint \bar{\bar{\mathbf{f}}} \cdot \hat{\mathbf{t}}\, W_i\, \mathrm{d}\ell \;+\; \iint \Big[-\bar{\bar{\mathbf{f}}} \cdot \widetilde{\nabla} W_i \;+\; \mathbf{q}\, W_i \;+\; \mu\,(\mathbf{g}-\boldsymbol{a})\, W_i \Big]\, \mathrm{d}\mathcal{A} \;=\; \mathbf{0} \tag{17}$$

$$\boldsymbol{\mathcal{R}}_i^m \;\equiv\; \oint \Big(\hat{\mathbf{d}}\times\bar{\bar{\mathbf{m}}} + \mathbf{r}\times\bar{\bar{\mathbf{f}}}\Big) \cdot \hat{\mathbf{t}}\, W_i\, \mathrm{d}\ell \;+\; \iint \Big[-\Big(\hat{\mathbf{d}}\times\bar{\bar{\mathbf{m}}} + \mathbf{r}\times\bar{\bar{\mathbf{f}}}\Big) \cdot \widetilde{\nabla} W_i \;+\; \mathbf{r}\times\mathbf{q}\, W_i \Big]\, \mathrm{d}\mathcal{A} \;=\; \mathbf{0} \tag{18}$$

For simplicity, the typically very small surface-stress and mass-moment torques $\hat{\mathbf{d}}\times\boldsymbol{\tau}$ and $\varsigma\hat{\mathbf{d}}\times(\mathbf{g}-\boldsymbol{a})$ have been dropped from (18), although if deemed significant they could be retained with no complications.

V. Surface Coordinates

Quantities in the element surface coordinate basis will use traditional tensor index notation, with ξ, η denoted as ξ^1, ξ^2, or compactly as ξ^α with $\alpha \in \{1, 2\}$. Coordinate derivatives will be compactly denoted by $\partial_\alpha(\,) \equiv \partial(\,)/\partial\xi^\alpha$. Also following convention, vector and tensor covariant and contravariant components associated with these coordinates will be denoted by subscript and superscript indices, respectively. Vectors and tensors in boldface will indicate coordinate-independent (invariant) quantities, although in the numerical implementation they are defined via their global cartesian xyz components.

A. Basis Vectors

C^0-SURFACE BASIS VECTORS. The simplest and conventional definition of the element covariant basis vectors is the ξ and η derivatives of the position vector $\overline{\mathbf{r}}(\xi,\eta)$.

$$\overline{\mathbf{a}}_\alpha(\xi,\eta) \;\equiv\; \partial_\alpha \overline{\mathbf{r}} \tag{19}$$

This makes $\overline{\mathbf{a}}_\alpha$ tangent to the "faceted" bilinearly interpolated surface, indicated in Figure 5.

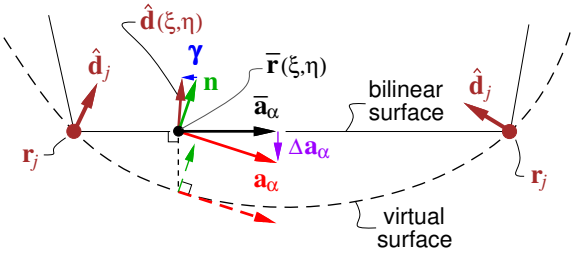

Figure 5. Basis vectors $\mathbf{a}_\alpha$ tangent to a virtual C^1-continuous surface.

C^1-SURFACE BASIS VECTORS. The higher-order basis vectors $\mathbf{a}_\alpha$ used in HSM are obtained by removing the components of $\mathbf{a}_\alpha$ along an estimated normal vector $\mathbf{n}$, and stretching by the factors K_α.

$$\mathbf{n}(\xi,\eta) \;\equiv\; \hat{\mathbf{d}} - \boldsymbol{\gamma} \tag{20}$$

$$\mathbf{a}_\alpha(\xi,\eta) \;\equiv\; K_\alpha \left[\, \overline{\mathbf{a}}_\alpha \;-\; \mathbf{n}\,(\mathbf{n}\cdot\overline{\mathbf{a}}_\alpha)\,\right] \tag{21}$$

$$K_\alpha \;=\; \frac{\overline{\mathbf{a}}_\alpha\cdot\overline{\mathbf{a}}_\alpha}{\overline{\mathbf{a}}_\alpha\cdot\overline{\mathbf{a}}_\alpha - (\mathbf{n}\cdot\overline{\mathbf{a}}_\alpha)^2} \tag{22}$$

This definition makes the change $\Delta\mathbf{a}_\alpha \equiv \mathbf{a}_\alpha - \overline{\mathbf{a}}_\alpha$ be orthogonal to $\overline{\mathbf{a}}_\alpha$, as indicated in Figure 5.

$$\Delta\mathbf{a}_\alpha\cdot\overline{\mathbf{a}}_\alpha \;=\; (\mathbf{a}_\alpha - \overline{\mathbf{a}}_\alpha)\cdot\overline{\mathbf{a}}_\alpha \;=\; 0$$

In the $\mathbf{n}$ definition (20), $\hat{\mathbf{d}}(\xi,\eta)$ is obtained via spherical interpolation, and the transverse shear stress vector $\boldsymbol{\gamma}(\xi,\eta)$ is obtained via MITC interpolation. These interpolations will be described later.

The definition (21) makes $\mathbf{a}_\alpha$ tangent to a virtual C^1-continuous surface which is everywhere normal to the $\mathbf{n}(\xi,\eta)$ field, as diagrammed in Figure 5. The stretching factors K_α also make $\mathbf{a}_\alpha$ give the metric tensor of the slightly longer curved virtual surface. Hence, when the shell is subjected to a pure bending deformation, the spacing between the nodes will shrink such that the arc length of the virtual surface is maintained to first order. This considerably improves accuracy for cases with large bending deformations.

Using the basis vectors we define the following surface metric, curvature, and director-lean tensors.

$$\breve{g}_{\alpha\beta} \;\equiv\; \mathbf{a}_\alpha\cdot\mathbf{a}_\beta \tag{23}$$

$$\breve{h}_{\alpha\beta} \;\equiv\; \mathbf{a}_\alpha\cdot\partial_\beta\hat{\mathbf{d}} \tag{24}$$

$$\breve{\ell}_\alpha \;\equiv\; \mathbf{a}_\alpha\cdot\hat{\mathbf{d}} \tag{25}$$

The metric determinant and its inverse $\breve{g}^{\alpha\beta}$ are defined by

$$\breve{g} \;\equiv\; \det(\breve{g}_{\alpha\beta}) \tag{26}$$

$$\breve{g}^{\alpha\beta} \;\equiv\; \left[\breve{g}_{\alpha\beta}\right]^{-1} \;=\; \frac{1}{\breve{g}}\begin{bmatrix}\breve{g}_{22} & -\breve{g}_{12}\\ -\breve{g}_{12} & \breve{g}_{11}\end{bmatrix} \tag{27}$$

which then give the contravariant basis vectors and the area element.

$$\mathbf{a}^\alpha = \breve{g}^{\alpha\beta}\,\mathbf{a}_\beta \tag{28}$$

$$\mathrm{d}\mathcal{A} = \sqrt{\breve{g}}\,\mathrm{d}\xi^1\,\mathrm{d}\xi^2 \tag{29}$$

We also apply all the above definitions (19)–(28) to the undeformed geometry $\mathbf{r}_{0(\xi^\alpha)}$, to give the corresponding $\mathbf{a}_{0_\alpha}$, $\breve{g}_{0_{\alpha\beta}}$, $\breve{h}_{0_{\alpha\beta}}$, $\breve{\ell}_{0_\alpha}$, $\breve{g}_0$, $\breve{g}_0^{\alpha\beta}$, and $\mathbf{a}_0^\alpha$. The undeformed area element is $\mathrm{d}\mathcal{A}_0 = \sqrt{\breve{g}_0}\,\mathrm{d}\xi^1\,\mathrm{d}\xi^2$.

B. Tangential Gradient

The tangential gradient of any scalar quantity on the surface is computed using its coordinate derivatives and the contravariant basis vectors, both defined on the virtual surface as described above.

$$\widetilde{\nabla}_{(\,)} = \mathbf{a}^1\,\partial_{1(\,)} + \mathbf{a}^2\,\partial_{2(\,)} \tag{30}$$

Gradients of in-surface vectors or tensors will not appear in the numerical solution method, which avoids the need to construct basis-vector gradients and associated Christoffel symbols.

C. Effective Shell Position Vector

In the angular momentum residual (18), bending moments are driven primarily by the transverse shear stresses, and also by the membrane stresses in curved shells, both acting over the position vector $\mathbf{r}$ which here serves as the moment arm. To improve accuracy for cases with large initial curvatures or large bending deformation, HSM defines this $\mathbf{r}$ to lie on a virtual surface which is offset from the bilinear surface $\bar{\mathbf{r}}$ as diagrammed in Figure 6. We have

$$\mathbf{r}_{(\xi,\eta)} = \bar{\mathbf{r}} + \left[B_1\phi_1(\xi) + B_2\phi_2(\eta)\right]\hat{\mathbf{n}}_c \tag{31}$$

where $\hat{\mathbf{n}}_c$ is a local normal vector, which will be conveniently defined at the element centroid. The ϕ_1, ϕ_2 "bubble" functions are defined to be zero at each node and quadratic over an element. Their coefficients B_1, B_2 are chosen so that the director field is nearly normal to the virtual surface. Specifically, we require

$$\min_{B_1,B_2} \iint \frac{1}{2}\left[\left(\hat{\mathbf{d}}\cdot\partial_1\mathbf{r}\right)^2 + \left(\hat{\mathbf{d}}\cdot\partial_2\mathbf{r}\right)^2\right]\mathrm{d}A \tag{32}$$

with the integral carried out over the element. Carrying out the minimization gives explicit expressions for the coefficients.

$$B_1 = \frac{-\iint \hat{\mathbf{d}}\cdot\partial_1\bar{\mathbf{r}}\;\partial_1\phi_1\,\mathrm{d}A}{\iint(\partial_1\phi_1)^2\,\mathrm{d}A} \quad , \qquad B_2 = \frac{-\iint \hat{\mathbf{d}}\cdot\partial_2\bar{\mathbf{r}}\;\partial_2\phi_2\,\mathrm{d}A}{\iint(\partial_2\phi_2)^2\,\mathrm{d}A} \tag{33}$$

The factors $\hat{\mathbf{d}}\cdot\hat{\mathbf{n}}_c$ have been dropped from the integrals for simplicity, since these are nearly unity and we are estimating a higher-order correction to begin with. For the same reason the director $\hat{\mathbf{d}}$ is being used rather than the more appropriate but more complicating estimated normal $\mathbf{n}$ given by (20). This is also justified by noting that a uniform transverse strain field would merely add a constant to the least-squares penalty function (32), with no effect on the resulting B_1, B_2 coefficients.

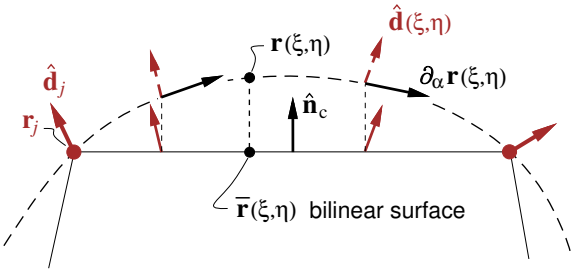

Figure 6. Effective shell position vector r offset from bilinear surface $\bar{\mathbf{r}}$, based on director $\hat{\mathbf{d}}$ distribution over an element.

D. Stress Tensor Decomposition

The stress integral resultant tensor is decomposed into in-surface and transverse parts,

$$\bar{\bar{\mathbf{f}}} \;=\; \bar{\bar{\mathbf{f}}}_S \,+\, \bar{\bar{\mathbf{f}}}_T \tag{34}$$

$$\bar{\bar{\mathbf{f}}}_S \;=\; \breve{f}^{\alpha\beta}\,\mathbf{a}_\alpha\mathbf{a}_\beta \;=\; \breve{f}^{11}\,\mathbf{a}_1\,\mathbf{a}_1 \,+\, \breve{f}^{12}\,(\mathbf{a}_1\,\mathbf{a}_2+\mathbf{a}_2\,\mathbf{a}_1) \,+\, \breve{f}^{22}\,\mathbf{a}_2\,\mathbf{a}_2 \tag{35}$$

$$\bar{\bar{\mathbf{f}}}_T \;=\; \breve{f}^{\alpha n}(\mathbf{a}_\alpha\hat{\mathbf{n}}+\hat{\mathbf{n}}\,\mathbf{a}_\alpha) \;=\; \breve{f}^{1n}\,(\mathbf{a}_1\,\hat{\mathbf{n}}+\hat{\mathbf{n}}\,\mathbf{a}_1) \,+\, \breve{f}^{2n}\,(\mathbf{a}_2\,\hat{\mathbf{n}}+\hat{\mathbf{n}}\,\mathbf{a}_2) \tag{36}$$

where each vector dyad denotes the usual outer product, i.e. $\mathbf{a}_1\,\mathbf{a}_2 = \mathbf{a}_1\,\mathbf{a}_2^{\mathsf{T}} = \mathbf{a}_1\otimes\mathbf{a}_2$. The remaining $\breve{f}^{nn}\,\hat{\mathbf{n}}\,\hat{\mathbf{n}}$ transverse normal-stress part is omitted, since this is assumed negligible within the thin-shell approximations.

The stress-moment integral resultant tensor is assumed to have the form

$$\bar{\bar{\mathbf{m}}} \;=\; \bar{\bar{\mathbf{m}}}_S \;=\; \breve{m}^{11}\,\mathbf{a}_1\,\mathbf{a}_1 \,+\, \breve{m}^{12}\,(\mathbf{a}_1\,\mathbf{a}_2+\mathbf{a}_2\,\mathbf{a}_1) \,+\, \breve{m}^{22}\,\mathbf{a}_2\,\mathbf{a}_2 \tag{37}$$

from which $\breve{m}^{1n}, \breve{m}^{2n}, \breve{m}^{nn}$ are omitted since these are negligible within the thin-shell approximation.

VI. Strains

As with the stresses, the strain tensor is decomposed into in-surface and transverse parts.

$$\bar{\bar{\boldsymbol{\varepsilon}}} \;=\; \bar{\bar{\boldsymbol{\varepsilon}}}_S \,+\, \bar{\bar{\boldsymbol{\varepsilon}}}_T \tag{38}$$

$$\bar{\bar{\boldsymbol{\varepsilon}}}_S \;=\; \breve{\varepsilon}_{\alpha\beta}\,\mathbf{a}^\alpha\mathbf{a}^\beta \tag{39}$$

$$\bar{\bar{\boldsymbol{\varepsilon}}}_T \;=\; \tfrac{1}{2}\breve{\gamma}_\alpha(\mathbf{a}^\alpha\hat{\mathbf{n}}+\hat{\mathbf{n}}\,\mathbf{a}^\alpha) \tag{40}$$

For a point $\mathbf{r}'$ at location ζ from the reference surface, defined by (1), the in-surface strain tensor is

$$\begin{aligned} \breve{\varepsilon}'_{\alpha\beta} \;&\equiv\; \tfrac{1}{2}\big(\breve{g}'_{\alpha\beta} - \breve{g}'_{0_{\alpha\beta}}\big) \\ &\simeq\; \breve{\varepsilon}_{\alpha\beta} \,+\, \zeta\,\breve{\kappa}_{\alpha\beta} \end{aligned} \tag{41}$$

where in the linearized form (41) the ζ^2 term was dropped as a thin-shell approximation. This is seen to have a membrane contribution $\breve{\varepsilon}_{\alpha\beta}$ due to tangential stretching and shearing of the reference surface, and a bending contribution $\breve{\kappa}_{\alpha\beta}$ due to curvature changes of the reference surface.

$$\breve{\varepsilon}_{\alpha\beta} \;\equiv\; \tfrac{1}{2}\big(\breve{g}_{\alpha\beta} - \breve{g}_{0_{\alpha\beta}}\big) \tag{42}$$

$$\breve{\kappa}_{\alpha\beta} \;\equiv\; \breve{h}_{\alpha\beta} - \breve{h}_{0_{\alpha\beta}} \tag{43}$$

$$\breve{\gamma}_\alpha \;\equiv\; \breve{\ell}_\alpha - \breve{\ell}_{0\alpha} \tag{44}$$

VII. Constitutive Relations

A. Stress-Strain Relations

The stress and strain tensors are related by assuming a Hookean material, with the in-surface and transverse tensors assumed to be decoupled. We substitute the strain (41) into the Hookean stress-strain relations,

$$\bar{\bar{\boldsymbol{\sigma}}}_S \;=\; \bar{\bar{\bar{\mathbf{c}}}} : \bar{\bar{\boldsymbol{\varepsilon}}}' \tag{45}$$

$$\bar{\bar{\boldsymbol{\sigma}}}_T \;=\; \bar{\bar{\mathbf{s}}} \cdot \boldsymbol{\gamma} \tag{46}$$

where $\bar{\bar{\bar{\mathbf{c}}}}$ is the 4th-rank in-surface stiffness tensor and $\bar{\bar{\mathbf{s}}}$ is the 2nd-rank transverse shear stiffness tensor. Integration across the shell thickness and transformation into the element basis then ultimately gives

$$\breve{f}^{\alpha\beta}{}_{(\xi,\eta)} \;=\; \breve{A}^{\alpha\beta\gamma\delta}\,\breve{\varepsilon}_{\gamma\delta} \,+\, \breve{B}^{\alpha\beta\gamma\delta}\,\breve{\kappa}_{\gamma\delta} \tag{47}$$

$$\breve{m}^{\alpha\beta}{}_{(\xi,\eta)} \;=\; \breve{B}^{\alpha\beta\gamma\delta}\,\breve{\varepsilon}_{\gamma\delta} \,+\, \breve{D}^{\alpha\beta\gamma\delta}\,\breve{\kappa}_{\gamma\delta} \tag{48}$$

$$\breve{f}^{\alpha n} \;=\; \breve{S}^{\alpha n}\,\breve{\gamma}_\alpha \tag{49}$$

where the matrices are 0th, 1st, and 2nd moments of the stiffnesses across the shell,

$$\breve{A} \,\equiv\, \int \breve{c}\,\mathrm{d}\zeta \quad , \qquad \breve{B} \,\equiv\, \int \breve{c}\,\zeta\,\mathrm{d}\zeta \quad , \qquad \breve{D} \,\equiv\, \int \breve{c}\,\zeta^2\,\mathrm{d}\zeta \quad , \qquad \breve{S} \,\equiv\, k\int \breve{s}\,\mathrm{d}\zeta \tag{50}$$

and k is the transverse strain energy reduction factor, equal to 5/6 for an isotropic shell. A balanced shell material with the reference surface at its midpoint has $\breve{B} = 0$, but in practice it is desirable to put the reference surface on one side which is the usual location of the body OML definition. So for generality, and for natural use with geometry representations, any assumptions on the reference surface placement are avoided here.

VIII. Finite-Element Solution

This section summarizes the Galerkin finite element solution method. All boldface vectors are numerically defined in the global cartesian xyz basis.

A. Global Data

The global data is listed in Table 1. For stationary problems, the only global parameter is the gravity acceleration vector $\mathbf{g}$. For non-stationary problems, additional parameters would be the frame velocity $\mathbf{U}_{(t)}$ at the xyz origin and frame rotation rate $\mathbf{\Omega}_{(t)}$, both sketched in Figure 1, and their corresponding rates $\dot{\mathbf{U}}_{(t)}$ and $\dot{\mathbf{\Omega}}_{(t)}$, all relative to some inertial frame of reference (e.g. earth). These can be either prescribed, as in a forced-motion case, or evolved in time via additional kinematic constraints and global momentum and angular-momentum conservation constraints, as in a free-body case.

Table 1. Specified global data

symbol	description
$\mathbf{g}$	gravity acceleration
$\mathbf{U}_{(t)}$	frame velocity
$\mathbf{\Omega}_{(t)}$	frame rotation rate
$\dot{\mathbf{U}}_{(t)}$	frame velocity time rate of change
$\dot{\mathbf{\Omega}}_{(t)}$	frame rotational acceleration

For a purely translating case, which has $\mathbf{\Omega} = \dot{\mathbf{\Omega}} = \mathbf{0}$, we can ignore $\mathbf{U}$. And in this case if $\dot{\mathbf{U}}$ is also constant in time, it can be lumped into a modified effective gravity vector

$$\mathbf{g} \;\leftarrow\; \mathbf{g} - \dot{\mathbf{U}}$$

and we can then set $\boldsymbol{a} = \mathbf{0}$ in residual (17).

B. Nodal Data

1. Parameters

In common CAD and FEM analysis practice, a complex undeformed geometry is defined by the parametric surface $\mathbf{r}_{0(u,v)}$, where u, v are the global (e.g. B-spline) surface coordinates. This also then uniquely defines the $\hat{\mathbf{n}}_{0(u,v)}$ distribution.

$$\hat{\mathbf{n}}_0 \;=\; \frac{\partial_u \mathbf{r}_0 \times \partial_v \mathbf{r}_0}{|\partial_u \mathbf{r}_0 \times \partial_v \mathbf{r}_0|} \tag{51}$$

The same u, v parameterization can be used for the shell material properties (stiffnesses, mass), and also the applied loads. After the shell discretization is chosen, this B-spline input data is evaluated at the discrete nodes. This makes the input data the same for triangle and quad elements, and also independent of the element integration schemes. All the required data values at each node j are listed in Table 2.

The stiffnesses in the table are most naturally specified in the chosen nodal $12n$ basis. For isotropic shell materials, the orientation of the $\hat{\mathbf{e}}_{0_1}, \hat{\mathbf{e}}_{0_2}$ vectors within the tangent plane is arbitrary, and an adequate choice is

$$\hat{\mathbf{e}}_{0_1} \;=\; \partial_u \mathbf{r}_0 \quad , \qquad \hat{\mathbf{e}}_{0_2} \;=\; \hat{\mathbf{n}}_0 \times \hat{\mathbf{e}}_{0_1} . \tag{52}$$

If the shell material is anisotropic with known properties along specific directions, such as a composite, then it is natural to orient $\hat{\mathbf{e}}_{0_1}, \hat{\mathbf{e}}_{0_2}$ along these directions, since this will then simplify the stiffness matrix specification.

Table 2. Specified nodal data

symbol	num.	axes	description
$\mathbf{r}_{0_j}$	3	xyz	position vector of undeformed geometry
$\bar{\bar{\mathbf{e}}}_{0_j}$	9	xyz	$\hat{\mathbf{e}}_{0_1}, \hat{\mathbf{e}}_{0_2}, \hat{\mathbf{n}}_0$ unit vectors of undeformed geometry
$\bar{\bar{A}}_j$	6	$12n$	lumped shell extension and shear stiffness
$\bar{\bar{B}}_j$	6	$12n$	lumped shell extension/bending coupling
$\bar{\bar{D}}_j$	6	$12n$	lumped shell bending stiffness
$\bar{\bar{S}}_j$	2	$12n$	lumped shell transverse shear stiffness
q_{n_j}	1	$12n$	shell-following applied normal force/area
$\mathbf{q}_{xyz_j}$	3	xyz	fixed-direction applied force/area
μ_j	1	—	lumped shell mass (mass/area density)

A typical shell-following load is the pressure difference across the top and bottom sides of the shell.

$$q_n \;=\; p_{\text{bot}} - p_{\text{top}} \tag{53}$$

A shell-following tangential shear load could also be imposed, although this is a vector and its basis vectors in the deformed configuration would be ambiguous.

2. Unknowns (primary variables)

The primary variables which are to be determined at each node j are listed in Table 3.

Table 3. Primary nodal unknowns

symbol	description
$\mathbf{r}_j$	position vector of deformed geometry
$\hat{\mathbf{d}}_j$	unit material vector (director) of deformed geometry

It should be noted that since each $\hat{\mathbf{d}}_j$ vector has unit magnitude, it actually represents two rather than three unknowns, which will be exploited later in the Newton method formulation. The resulting numerical problem will then have a total of 5 or 8 unknowns per node for steady or unsteady cases, respectively.

C. Element Interpolation

1. Bilinear interpolation

The nodal $\mathbf{r}_j$ variables are interpolated to the element interior by usual bilinear interpolation, which also gives their covariant derivatives.

$$\bar{\mathbf{r}}_{(\xi,\eta)} \;=\; \textstyle\sum_j \mathbf{r}_j \, N_j \tag{54}$$

$$\partial_\alpha \bar{\mathbf{r}}_{(\xi,\eta)} \;=\; \textstyle\sum_j \mathbf{r}_j \, \partial_\alpha N_j \tag{55}$$

The interpolation functions used for quad and triangular elements are listed below.

$$\begin{aligned} N_{1(\xi,\eta)} &= \tfrac{1}{4}(1-\xi)(1-\eta) \\ N_{2(\xi,\eta)} &= \tfrac{1}{4}(1+\xi)(1-\eta) \\ N_{3(\xi,\eta)} &= \tfrac{1}{4}(1+\xi)(1+\eta) \\ N_{4(\xi,\eta)} &= \tfrac{1}{4}(1-\xi)(1+\eta) \end{aligned} \qquad \text{(quad)} \qquad\qquad \begin{aligned} N_{1(\xi,\eta)} &= 1-\xi-\eta \\ N_{2(\xi,\eta)} &= \xi \\ N_{3(\xi,\eta)} &= \eta \end{aligned} \qquad \text{(triangle)} \tag{56}$$

Bilinear interpolation of the nodal normal vectors $\hat{\mathbf{d}}_j$ does not in general produce a unit vector. A common fix is to combine it with normalization,

$$\hat{\mathbf{d}}_{(\xi,\eta)} \;=\; \frac{\sum_j \hat{\mathbf{d}}_j\, N_j}{\left|\sum_j \hat{\mathbf{d}}_j\, N_j\right|} \tag{57}$$

although this will still produce irregularities in $\hat{\mathbf{d}}_{(\xi,\eta)}$ for very a highly curved element.

2. Spherical interpolation

To minimize sensitivity to element curvature HSM uses spherical interpolation. An element reference unit vector $\hat{\mathbf{d}}_{\rm ref}$ is first defined, with the first node's ($j=1$) vector being a convenient choice.

$$\hat{\mathbf{d}}_{\rm ref} \;=\; \hat{\mathbf{d}}_1 \tag{58}$$

This is then used to define the log-quaternion $\boldsymbol{\lambda}_j$ for each node, which is half the rotation vector needed to rotate $\hat{\mathbf{d}}_{\rm ref}$ into $\hat{\mathbf{d}}_j$, as shown in the diagram below.

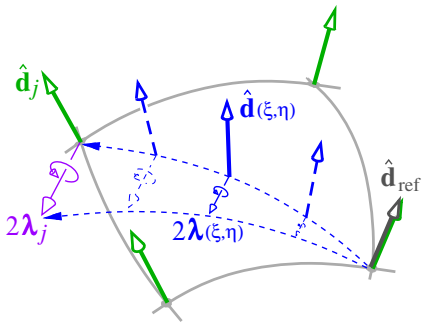

$$\boldsymbol{\alpha}_j \;=\; \hat{\mathbf{d}}_{\rm ref} \times \hat{\mathbf{d}}_j \tag{59}$$

$$\theta_j \;=\; \mathrm{atan2}\Big(\, |\boldsymbol{\alpha}_j| \;,\; \hat{\mathbf{d}}_{\rm ref} \cdot \hat{\mathbf{d}}_j \,\Big) \tag{60}$$

$$\boldsymbol{\lambda}_j \;=\; \begin{cases} \mathbf{0} & ,\quad |\boldsymbol{\alpha}_j| = 0 \\ \dfrac{\boldsymbol{\alpha}_j}{|\boldsymbol{\alpha}_j|}\,\dfrac{\theta_j}{2} & ,\quad |\boldsymbol{\alpha}_j| \neq 0 \end{cases} \tag{61}$$

These nodal $\boldsymbol{\lambda}_j$ values are interpolated over the element using the interpolation functions,

$$\boldsymbol{\lambda}_{(\xi,\eta)} \;=\; \textstyle\sum_j \boldsymbol{\lambda}_j\, N_j \tag{62}$$

and this is then used to rotate $\hat{\mathbf{d}}_{\rm ref}$ into $\hat{\mathbf{d}}_{(\xi,\eta)}$ which is the required result.

$$w_{(\xi,\eta)} \;=\; \cos|\boldsymbol{\lambda}| \;\;\simeq\;\; 1 - \tfrac{1}{2}|\boldsymbol{\lambda}|^2 \tag{63}$$

$$\mathbf{v}_{(\xi,\eta)} \;=\; \frac{\sin|\boldsymbol{\lambda}|}{|\boldsymbol{\lambda}|}\,\boldsymbol{\lambda} \;\simeq\; \left(1 - \tfrac{1}{6}|\boldsymbol{\lambda}|^2\right)\boldsymbol{\lambda} \tag{64}$$

$$\hat{\mathbf{d}}_{(\xi,\eta)} \;=\; \hat{\mathbf{d}}_{\rm ref} \;+\; 2\,\mathbf{v} \times \Big(\mathbf{v} \times \hat{\mathbf{d}}_{\rm ref} \;+\; w\,\hat{\mathbf{d}}_{\rm ref}\Big) \tag{65}$$

The coordinate derivatives of $\hat{\mathbf{d}}_{(\xi,\eta)}$ are obtained by explicit differentiation of the above expressions.

$$\partial_\alpha \boldsymbol{\lambda} \;=\; \textstyle\sum_j \boldsymbol{\lambda}_j\, \partial_\alpha N_j \tag{66}$$

$$\partial_\alpha w \;=\; -\frac{\sin|\boldsymbol{\lambda}|}{|\boldsymbol{\lambda}|}\,\boldsymbol{\lambda}\cdot\partial_\alpha\boldsymbol{\lambda} \qquad\qquad \simeq\; -\boldsymbol{\lambda}\cdot\partial_\alpha\boldsymbol{\lambda} \tag{67}$$

$$\partial_\alpha \mathbf{v} \;=\; \frac{\sin|\boldsymbol{\lambda}|}{|\boldsymbol{\lambda}|}\,\partial_\alpha\boldsymbol{\lambda} \;+\; \left(\cos|\boldsymbol{\lambda}| - \frac{\sin|\boldsymbol{\lambda}|}{|\boldsymbol{\lambda}|}\right)\frac{\boldsymbol{\lambda}}{|\boldsymbol{\lambda}|^2}\,\boldsymbol{\lambda}\cdot\partial_\alpha\boldsymbol{\lambda} \;\simeq\; \left(1 - \tfrac{1}{6}|\boldsymbol{\lambda}|^2\right)\partial_\alpha\boldsymbol{\lambda} \tag{68}$$

$$\partial_\alpha \hat{\mathbf{d}} \;=\; 2\,\partial_\alpha\mathbf{v} \times \Big(\mathbf{v} \times \hat{\mathbf{d}}_{\rm ref} \;+\; w\,\hat{\mathbf{d}}_{\rm ref}\Big) \;+\; 2\,\mathbf{v} \times \Big(\partial_\alpha\mathbf{v} \times \hat{\mathbf{d}}_{\rm ref} \;+\; \partial_\alpha w\;\hat{\mathbf{d}}_{\rm ref}\Big) \tag{69}$$

The approximate forms in (63), (64), (67), (68), are used when $|\boldsymbol{\lambda}|^2 < \epsilon_{\rm machine}$ to prevent a divide by zero.

Operations (58)–(69) are also applied to the undeformed-geometry $\hat{\mathbf{n}}_{0_j}$ vectors to obtain the interpolated $\hat{\mathbf{n}}_{0(\xi,\eta)}$ vector and its covariant derivatives $\partial_\alpha\hat{\mathbf{n}}_0$.

3. Transverse shear strain interpolation

The transverse strain defined by HSM is based on the standard MITC formulation,[3] with interpolation from the edge midpoints rather than from the corner nodes. One modification here is that the edge-midpoint $\hat{\mathbf{d}}_{j+1/2}$ values are obtained using spherical interpolation between the j and $j+1$ nodes, specifically by using

$$\boldsymbol{\lambda}_{j+1/2} \;=\; \tfrac{1}{2}\,(\boldsymbol{\lambda}_{j+1} + \boldsymbol{\lambda}_j) \tag{70}$$

in expressions (63)–(65). For each edge midpoint we then compute

$$\breve{\gamma}_{\alpha_{j+1/2}} \;=\; \overline{\mathbf{a}}_{\alpha_{j+1/2}} \cdot \hat{\mathbf{d}}_{j+1/2} \;-\; \overline{\mathbf{a}}_{0_{\alpha_{j+1/2}}} \cdot \hat{\mathbf{n}}_{0_{j+1/2}} \tag{71}$$

and these are then interpolated using the following standard MITC scheme to give the $\breve{\gamma}_{\alpha(\xi,\eta)}$ field for a quad element.

$$\breve{\gamma}_{1(\eta)} \;=\; \tfrac{1}{2}(1-\eta)\,\breve{\gamma}_{1_{1\,1/2}} \;-\; \tfrac{1}{2}(1+\eta)\,\breve{\gamma}_{1_{3\,1/2}} \tag{72}$$

$$\breve{\gamma}_{2(\xi)} \;=\; \tfrac{1}{2}(1-\xi)\,\breve{\gamma}_{2_{4\,1/2}} \;-\; \tfrac{1}{2}(1+\xi)\,\breve{\gamma}_{2_{2\,1/2}} \tag{73}$$

The similar MITC3 scheme is used for triangular elements.[6] To compute the cartesian shear stress vector, we use the approximate (bilinear) contravariant basis vectors.

$$\boldsymbol{\gamma} \;=\; \breve{\gamma}_1\,\overline{\mathbf{a}}^1 \;+\; \breve{\gamma}_2\,\overline{\mathbf{a}}^2 \tag{74}$$

Once $\overline{\mathbf{r}}$, $\hat{\mathbf{d}}$, and $\boldsymbol{\gamma}$ are computed, the normal vector $\mathbf{n}$ and the virtual-surface $\mathbf{a}_\alpha$ basis vectors are computed using relations (20)–(22). The metric tensors and contravariant vectors $\mathbf{a}^\alpha$ are then obtained using (23)–(28)

4. Rotated nodal data

The stiffnesses of isotropic materials can be uniquely defined by the scalars E, ν (or equivalent Lamé constants), which allows stiffness properties to be constructed locally within the element. However, the shell stiffness properties for composite materials are inherently tensor quantities which must be defined in some basis, which here is chosen to be defined by the $\hat{\mathbf{e}}_{0_1}, \hat{\mathbf{e}}_{0_2}, \hat{\mathbf{n}}_0$ basis vectors tangent and normal to the surface. For a curved geometry these must in general differ between the nodes of an element, so the tensor stiffness data must be interpolated in some common basis. To exactly represent uniform loading and uniform strain and stress fields (and thus pass patch tests), this interpolation is typically performed in a local surface-aligned cartesian basis defined by the $\hat{\mathbf{c}}$ vectors computed at the element centroid[3,8] as follows.

$$\hat{\mathbf{c}}_{1_{\text{ref}}} \;=\; \left.\frac{\partial_\xi \mathbf{r}_0}{|\partial_\xi \mathbf{r}_0|}\right|_{\xi_c,\eta_c} \quad , \qquad \hat{\mathbf{c}}_{n_{\text{ref}}} \;=\; \left.\frac{\partial_\xi \mathbf{r}_0 \times \partial_\eta \mathbf{r}_0}{|\partial_\xi \mathbf{r}_0 \times \partial_\eta \mathbf{r}_0|}\right|_{\xi_c,\eta_c} \quad , \qquad \hat{\mathbf{c}}_{2_{\text{ref}}} \;=\; \hat{\mathbf{c}}_{n_{\text{ref}}} \times \hat{\mathbf{c}}_{1_{\text{ref}}} \tag{75}$$

For an element whose undeformed shape is curved, or more precisely whose nodal $\hat{\mathbf{n}}_0$ are not all parallel, using this basis as-is at the nodes will produce spurious cosine-error "mixing" between the tangential and normal components of the tensor node data, as suggested by the top diagram Figure 7 for the 2D case. In HSM this is avoided by using a rotated basis $\hat{\mathbf{c}}_j$ at each node, as indicated in the bottom diagram.

In the 3D case, the rotation is performed via equations (59)–(65), but now the rotation angle is what's required to rotate $\hat{\mathbf{c}}_{n_{\text{ref}}}$ into $\hat{\mathbf{n}}_{0_j}$, and no interpolation (via $\boldsymbol{\lambda}$) is needed.

$$\boldsymbol{\alpha} \;=\; \hat{\mathbf{c}}_{n_{\text{ref}}} \times \hat{\mathbf{n}}_{0_j} \tag{76}$$

$$\theta \;=\; \text{atan2}\Big(\; |\boldsymbol{\alpha}| \;,\; \hat{\mathbf{c}}_{n_{\text{ref}}} \cdot \hat{\mathbf{n}}_{0_j} \;\Big) \tag{77}$$

$$w \;=\; \cos(\theta/2) \tag{78}$$

$$\mathbf{v} \;=\; \frac{\boldsymbol{\alpha}}{|\boldsymbol{\alpha}|}\,\sin(\theta/2) \tag{79}$$

$$\hat{\mathbf{c}}_{1_j} \;=\; \hat{\mathbf{c}}_{1_{\text{ref}}} \;+\; 2\,\mathbf{v} \times \big(\mathbf{v} \times \hat{\mathbf{c}}_{1_{\text{ref}}} \;+\; w\,\hat{\mathbf{c}}_{1_{\text{ref}}}\big) \tag{80}$$

$$\hat{\mathbf{c}}_{2_j} \;=\; \hat{\mathbf{c}}_{2_{\text{ref}}} \;+\; 2\,\mathbf{v} \times \big(\mathbf{v} \times \hat{\mathbf{c}}_{2_{\text{ref}}} \;+\; w\,\hat{\mathbf{c}}_{2_{\text{ref}}}\big) \tag{81}$$

$$\hat{\mathbf{c}}_{n_j} \;=\; \hat{\mathbf{n}}_{0_j} \tag{82}$$

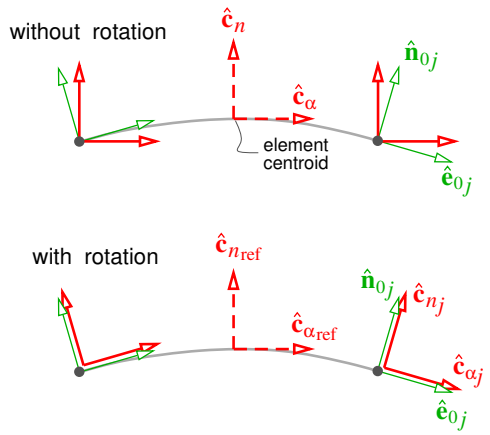

Figure 7. Rotation of 2D element cartesian $\hat{\mathbf{c}}$ basis vectors into each node avoids spurious mixing between tangential and normal components of node tensor data.

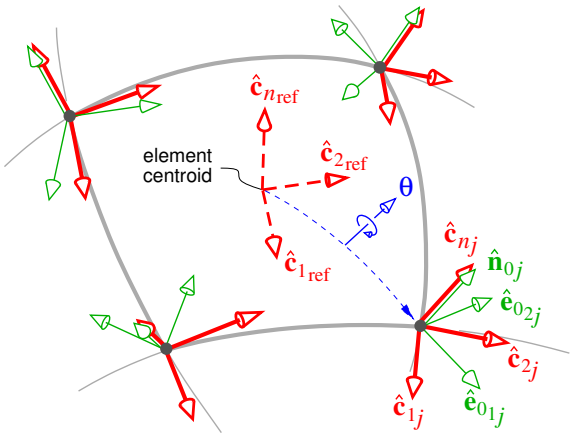

Figure 8. Cartesian $\hat{\mathbf{c}}_{\rm ref}$ basis vectors at element centroid of the undeformed geometry are rotated to each node j by the angle from $\hat{\mathbf{c}}_{n_{\rm ref}}$ to $\hat{\mathbf{n}}_{0_j}$. Nodal vector and tensor data is projected onto the rotated basis for interpolation over element.

These procedures are applied to each node of the element, as diagrammed in Figure 8. The components of the nodal stiffness tensors in the rotated element cartesian basis are

$$A^{\hat{\mathbf{c}}}_{abcd} = A_{ijk\ell}\,(\hat{\mathbf{e}}_{0_i}\cdot\hat{\mathbf{c}}_a)\,(\hat{\mathbf{e}}_{0_j}\cdot\hat{\mathbf{c}}_b)\,(\hat{\mathbf{e}}_{0_k}\cdot\hat{\mathbf{c}}_c)\,(\hat{\mathbf{e}}_{0_\ell}\cdot\hat{\mathbf{c}}_d) \tag{83}$$

$$S^{\hat{\mathbf{c}}}_{anbn} = S_{injn}\,(\hat{\mathbf{e}}_{0_i}\cdot\hat{\mathbf{c}}_a)\,(\hat{\mathbf{e}}_{0_j}\cdot\hat{\mathbf{c}}_b) \tag{84}$$

where here $i,j,k,\ell,a,b,c,d \in \{1,2\}$. These projected values are then interpolated to the interior as usual.

$$A^{\hat{\mathbf{c}}}_{abcd(\xi,\eta)} = \textstyle\sum_j (A^{\hat{\mathbf{c}}}_{abcd})_j\, N_j \;\;,\;\; \text{etc.} \tag{85}$$

Finally, the interpolated stiffnesses are put into the local contravariant basis.

$$\breve{A}^{\alpha\beta\gamma\delta} = A^{\hat{\mathbf{c}}}_{abcd}\,(\hat{\mathbf{c}}_a\cdot\mathbf{a}_0^\alpha)\,(\hat{\mathbf{c}}_b\cdot\mathbf{a}_0^\beta)\,(\hat{\mathbf{c}}_c\cdot\mathbf{a}_0^\gamma)\,(\hat{\mathbf{c}}_d\cdot\mathbf{a}_0^\delta) \tag{86}$$

$$\breve{S}^{\alpha n\beta n} = S^{\hat{\mathbf{c}}}_{anbn}\,(\hat{\mathbf{c}}_a\cdot\mathbf{a}_0^\alpha)\,(\hat{\mathbf{c}}_b\cdot\mathbf{a}_0^\beta) \tag{87}$$

Note that all these projections involve only the undeformed reference configuration and do not depend on the solution, so they could be performed only once for each element and stored.

5. Derived data and dependent variables

The total applied load $\mathbf{q}$ is the sum of the fixed-direction and shell-following normal loads.

$$\mathbf{q} = \mathbf{q}_{xyz} + q_n\,\hat{\mathbf{n}} \tag{88}$$

A *static* problem is one where $\boldsymbol{a}_o$ is constant in time, making the solution in the xyz frame steady. In this case the local acceleration $\boldsymbol{a}$ at location $\mathbf{r}$ is

$$\boldsymbol{a} \;=\; \dot{\mathbf{U}} \,+\, \boldsymbol{\Omega}\times\mathbf{U} \,+\, \dot{\boldsymbol{\Omega}}\times\mathbf{r} \,+\, \boldsymbol{\Omega}\times(\boldsymbol{\Omega}\times\mathbf{r}) \tag{89}$$

where the first two terms are the frame linear acceleration, the third term is the relative tangential acceleration, and the last term is the relative centripetal acceleration. General dynamic problems require the introduction of a node velocity $\mathbf{u}$ as a primary unknown, which adds $\dot{\mathbf{u}} + 2\,\boldsymbol{\Omega}\times\mathbf{u}$ to the acceleration (89). This extension will not be considered here.

The interior metric and curvature tensors are used to compute the strain and curvature-change tensors. These and the stiffnesses then give the stress resultants as follows.

$$\breve{\varepsilon}_{\alpha\beta(\xi,\eta)} \;=\; \tfrac{1}{2}\left(\breve{g}_{\alpha\beta} - \breve{g}_{0_{\alpha\beta}}\right) \tag{90}$$

$$\breve{\kappa}_{\alpha\beta(\xi,\eta)} \;=\; \breve{h}_{\alpha\beta} - \breve{h}_{0_{\alpha\beta}} \tag{91}$$

$$\breve{f}^{\alpha\beta}{}_{(\xi,\eta)} \;=\; \breve{A}^{\alpha\beta\gamma\delta}\,\breve{\varepsilon}_{\gamma\delta} \,+\, \breve{B}^{\alpha\beta\gamma\delta}\,\breve{\kappa}_{\gamma\delta} \tag{92}$$

$$\breve{m}^{\alpha\beta}{}_{(\xi,\eta)} \;=\; \breve{B}^{\alpha\beta\gamma\delta}\,\breve{\varepsilon}_{\gamma\delta} \,+\, \breve{D}^{\alpha\beta\gamma\delta}\,\breve{\kappa}_{\gamma\delta} \tag{93}$$

$$\breve{f}^{\alpha n} \;=\; \breve{S}^{\alpha\beta}\,\breve{\gamma}_{\beta} \tag{94}$$

D. Equation Residuals

1. *Residual weights and integration*

HSM uses a standard Galerkin-type finite-element formulation, where the residual weighting function $W_{i(\xi,\eta)}$ associated with node i is chosen to be the "tent" function formed from the union of the $N_{i(\xi,\eta)}$ interpolants, shown in Figure 9. On each element we then have

$$W_{i\,(\xi,\eta)} \;=\; N_{i\,(\xi,\eta)} \tag{95}$$

$$\widetilde{\nabla} W_{i\,(\xi,\eta)} \;=\; \widetilde{\nabla} N_{i\,(\xi,\eta)} \tag{96}$$

where the weight function gradient $\widetilde{\nabla} W_i$ is defined via its element-basis components like $\widetilde{\nabla} N_i$.

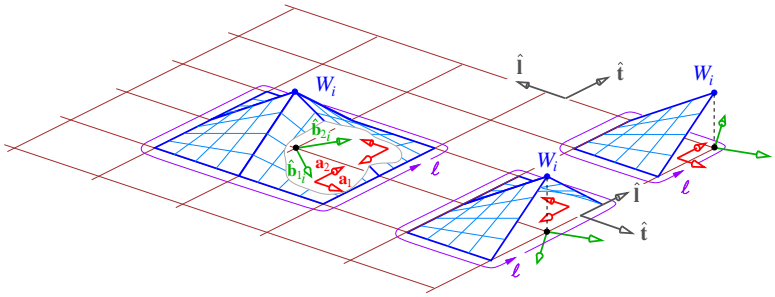

Figure 9. Residual weighting functions $W_{i(\xi,\eta)}$, variable and residual projection vectors $\hat{\mathbf{b}}_{1_i}, \hat{\mathbf{b}}_{2_i(\xi,\eta)}$, and element basis vectors $\mathbf{a}_1, \mathbf{a}_{2(\xi,\eta)}$ associated with interior, edge, and corner nodes. The edge-normal and edge-parallel tangent vectors $\hat{\mathbf{t}}, \hat{\mathbf{l}}$ and edge length coordinate ℓ are also shown.

Per standard procedure, all area integrals will be recast in terms of the element coordinates ξ, η and their Jacobian J_0, and then numerically evaluated using 4-point Gaussian quadrature,

$$\iint \mathcal{F}\,\mathrm{d}\mathcal{A}_0 \;=\; \iint \mathcal{F}\,J_0\;\mathrm{d}\xi\,\mathrm{d}\eta \;\simeq\; \sum_{k=1}^{4} \mathcal{F}_{(\xi_k,\eta_k)}\,J_{0(\xi_k,\eta_k)}\;w_k \tag{97}$$

$$J_0 \;=\; \left|\,\mathbf{a}_{0_1}\times\mathbf{a}_{0_2}\right| \tag{98}$$

where the index k runs over the Gauss points (ξ_k, η_k) and w_k are the corresponding Gauss weights. The integration is performed over the undeformed geometry, primarily because this simplifies linearization of the resulting residual expressions for Newton solution.

For the edge line integrals appearing in (17) and (18), 2-point Gaussian integration is used.

$$\int \mathcal{F}\,\mathrm{d}\ell_0 \;=\; \int \mathcal{F}\,J_0\;\mathrm{d}\xi \;\simeq\; \sum_{k=1}^{2} \mathcal{F}_{(\xi_k)}\,J_0\;w_k \tag{99}$$

Here, $-1 \le \xi \le +1$ is the parameter along the edge, and the Jacobian is a constant $J_0 = \Delta\ell_0/2$ where $\Delta\ell_0$ is the edge length of the undeformed element. The integrands are computed as

$$\bar{\bar{\mathbf{f}}}\cdot\hat{\mathbf{t}} \;\equiv\; \mathbf{f}_{\mathrm{BC}(\ell)} \;=\; \mathbf{f}_{xyz_{\mathrm{BC}}} \;+\; f_{t_{\mathrm{BC}}}\,\hat{\mathbf{t}} \;+\; f_{\ell_{\mathrm{BC}}}\,\hat{\mathbf{l}} \;+\; f_{n_{\mathrm{BC}}}\hat{\mathbf{d}} \tag{100}$$

$$\hat{\mathbf{d}}\times\bar{\bar{\mathbf{m}}}\cdot\hat{\mathbf{t}} \;\equiv\; \mathbf{m}_{\mathrm{BC}(\ell)} \;=\; \mathbf{m}_{xyz_{\mathrm{BC}}} \;+\; m_{t_{\mathrm{BC}}}\hat{\mathbf{t}} \;+\; m_{\ell_{\mathrm{BC}}}\hat{\mathbf{l}} \tag{101}$$

where all the components are provided by load boundary condition data.

E. Variable and Residual Projection Vectors

1. *Projection vector definitions*

To minimize the number of unknowns, and to enable the imposition of strong (Dirichlet) boundary conditions, we define local *projection basis vectors* $\hat{\mathbf{b}}_{1_i}$, $\hat{\mathbf{b}}_{2_i}$, $\hat{\mathbf{b}}_{n_i}$ at each discrete node i. It is desirable that these vectors are orthogonal, which will then minimize the coupling between the projected equations, but this is not required — they only need to be non-coplanar.

For all nodes, we define

$$\hat{\mathbf{b}}_{n_i} \;=\; \hat{\mathbf{d}}_i \tag{102}$$

and then define the remaining two vectors depending on where node i lies. For interior nodes, and edge nodes which have only loading boundary conditions, $\hat{\mathbf{b}}_{1_i}$ and $\hat{\mathbf{b}}_{2_i}$ are arbitrary as long as they span the shell reference surface. For numerical stability we choose $\hat{\mathbf{b}}_{1_i}$ to be the unit vector which is along the smallest component of $\hat{\mathbf{d}}_i = d_{x_i}\,\hat{\mathbf{x}} + d_{y_i}\,\hat{\mathbf{y}} + d_{z_i}\,\hat{\mathbf{z}}$, and orthogonalize it against $\hat{\mathbf{d}}_i$. We then set $\hat{\mathbf{b}}_{2_i}$ perpendicular to both $\hat{\mathbf{d}}_i$ and $\hat{\mathbf{b}}_{1_i}$.

For boundary nodes with one or two specified displacements along specified directions (e.g. normal to a symmetry plane), we set $\hat{\mathbf{b}}_{1_i}$ and/or $\hat{\mathbf{b}}_{2_i}$ along those directions, and orthogonalize any remaining unspecified $\hat{\mathbf{b}}$ vectors.

2. *Residual projection*

Each vector residual, including any loading BC contribution, is projected onto the $\hat{\mathbf{b}}_{1_i}, \hat{\mathbf{b}}_{2_i}, \hat{\mathbf{b}}_{n_i}$ vectors of the corresponding node.

$$\begin{Bmatrix} \mathcal{R}_i^{f_1} \\ \mathcal{R}_i^{f_2} \\ \mathcal{R}_i^{f_n} \end{Bmatrix} \;\equiv\; \begin{bmatrix} - & \hat{\mathbf{b}}_{1_i} & - \\ - & \hat{\mathbf{b}}_{2_i} & - \\ - & \hat{\mathbf{b}}_{n_i} & - \end{bmatrix} \cdot \begin{Bmatrix} | \\ \boldsymbol{\mathcal{R}}_i^{f} \\ | \end{Bmatrix} \tag{103}$$

$$\begin{Bmatrix} \mathcal{R}_i^{m_1} \\ \mathcal{R}_i^{m_2} \end{Bmatrix} \;\equiv\; \begin{bmatrix} - & \hat{\mathbf{b}}_{1_i} & - \\ - & \hat{\mathbf{b}}_{2_i} & - \end{bmatrix} \cdot \begin{Bmatrix} | \\ \boldsymbol{\mathcal{R}}_i^{m} \\ | \end{Bmatrix} \tag{104}$$

Equation (104) excludes the $\hat{\mathbf{b}}_{n_i}$ projection because the $\boldsymbol{\mathcal{R}}^m$ vector residual does not contain any $\hat{\mathbf{d}}$ component to first order. It would be retained if a director drilling degree of freedom were introduced into the formulation.

3. *Variable projection*

The projection vectors are also used to define perturbations of the primary vector variables,

$$\delta\mathbf{r}_i \;=\; \hat{\mathbf{b}}_{1_i}\,\delta r_{1_i} \;+\; \hat{\mathbf{b}}_{2_i}\,\delta r_{2_i} \;+\; \hat{\mathbf{b}}_{n_i}\,\delta r_{3_i} \tag{105}$$

$$\delta\hat{\mathbf{d}}_i \;=\; \hat{\mathbf{b}}_{1_i}\,\delta d_{1_i} \;+\; \hat{\mathbf{b}}_{2_i}\,\delta d_{2_i} \tag{106}$$

which can represent either the linearized variables in a perturbation analysis, or the variable changes in a Newton iteration solution procedure. Since $\hat{\mathbf{d}}_i$ is defined to be a unit vector, and with definition (102), we have $\delta d_{3_i} = 0$ a priori, thus reducing the number of Newton change variables from 6 to 5, i.e. from $(\delta\mathbf{r}, \delta\hat{\mathbf{d}})_i$ to $(\delta r_1, \delta r_2, \delta r_n, \delta d_1, \delta d_2)_i$.

A necessary precaution during solution iteration is that each $\hat{\mathbf{d}}_i$ must maintain its unit magnitude. This is ensured by rescaling each $\hat{\mathbf{d}}_i$ to unit magnitude after its Newton update, as follows.

$$\mathbf{d}_i^* \;=\; \hat{\mathbf{d}}_i \;+\; \hat{\mathbf{b}}_{1_i}\,\delta d_{1_i} \;+\; \hat{\mathbf{b}}_{2_i}\,\delta d_{2_i} \qquad , \qquad \hat{\mathbf{d}}_i \;=\; \mathbf{d}_i^* \,/\, |\mathbf{d}_i^*| \tag{107}$$

Since $|\mathbf{d}^*| = 1 + \mathcal{O}(\delta d^2)$, the effect of this explicit normalization vanishes as the solution is approached, so there is no noticeable adverse effect on the quadratic convergence of the Newton iteration.

F. Edge Geometry Boundary Conditions

As mentioned previously, the edge position or angle boundary conditions are of the Dirichlet type, and are imposed by replacing the appropriate natural residuals with the Dirichlet constraint residuals.

1. *Dirichlet boundary condition data*

All the boundary condition data which can be imposed on the shell edge nodes is listed in the table below. The edge position is specified by $\mathbf{r}_{\text{BC}}$ which is arbitrary, although in most cases it will be the same as $\mathbf{r}_0$ of the undeformed geometry. The edge orientation is specified by the $\mathbf{t}_{\text{BC}}, \mathbf{l}_{\text{BC}}$ vectors which are also arbitrary, but frequently same as $\hat{\mathbf{t}}_0$ and $\hat{\mathbf{l}}_0$.

2. *Target equations for Dirichlet boundary conditions*

After the projections onto $\hat{\mathbf{b}}_1, \hat{\mathbf{b}}_2, \hat{\mathbf{b}}_n$ are applied, each variable is predominantly governed by a Poisson-type equation which reduces to a Neumann BC on the boundary. To impose a Dirichlet BC on a variable in a well-posed manner, the Dirichlet BC residual must replace the corresponding Neumann BC residual, as listed in the table below.

$$\begin{aligned}
\mathcal{R}^{f_1} &\sim \hat{\mathbf{t}} \cdot \widetilde{\nabla} r_1 \quad &\rightarrow \quad \mathcal{R}^{r_1} &\sim r_1 \\
\mathcal{R}^{f_2} &\sim \hat{\mathbf{t}} \cdot \widetilde{\nabla} r_2 \quad &\rightarrow \quad \mathcal{R}^{r_2} &\sim r_2 \\
\mathcal{R}^{f_n} &\sim \hat{\mathbf{t}} \cdot \widetilde{\nabla} r_n \quad &\rightarrow \quad \mathcal{R}^{r_n} &\sim r_n \\
\mathcal{R}^{m_1} &\sim \hat{\mathbf{t}} \cdot \widetilde{\nabla} d_1 \quad &\rightarrow \quad \mathcal{R}^{d_1} &\sim d_1 \\
\mathcal{R}^{m_2} &\sim \hat{\mathbf{t}} \cdot \widetilde{\nabla} d_2 \quad &\rightarrow \quad \mathcal{R}^{d_2} &\sim d_2
\end{aligned}$$

Specifically, $\mathcal{R}^{r_1}$ must replace $\mathcal{R}^{f_1}$, $\mathcal{R}^{r_2}$ must replace $\mathcal{R}^{f_2}$, etc.

NODE DISPLACEMENT. The specified position of node i is imposed by replacing the two in-surface force equilibrium residuals and the single compatibility residual with the following three position-constraint residuals $\mathcal{R}_i^r$.

$$\begin{Bmatrix} \mathcal{R}_i^{f_1} \\ \mathcal{R}_i^{f_2} \\ \mathcal{R}_i^{\theta} \end{Bmatrix} \;\leftarrow\; \begin{Bmatrix} \mathcal{R}_i^{r_1} \\ \mathcal{R}_i^{r_2} \\ \mathcal{R}_i^{r_n} \end{Bmatrix} \;\equiv\; \begin{bmatrix} - & \hat{\mathbf{b}}_{1_i} & - \\ - & \hat{\mathbf{b}}_{2_i} & - \\ - & \hat{\mathbf{b}}_{n_i} & - \end{bmatrix} \cdot \begin{Bmatrix} | \\ \mathbf{r}_i - \mathbf{r}_{\text{BC}_i} \\ | \end{Bmatrix} \tag{108}$$

Either one or two or three of these residuals can be imposed, as dictated by the number of restrained degrees of freedom in the physical boundary condition.

NODE EDGE DIRECTION. The shell surface angles are imposed by requiring the shell material quasi-normal vector to lie within the specified sliding plane defined by either the $\hat{\mathbf{b}}_1$ or $\hat{\mathbf{b}}_2$ vector. The corresponding residuals replace the moment equilibrium equations.

$$\begin{Bmatrix} \mathcal{R}_i^{m_1} \\ \mathcal{R}_i^{m_2} \end{Bmatrix} \;\leftarrow\; \begin{Bmatrix} \mathcal{R}_i^{d_1} \\ \mathcal{R}_i^{d_2} \end{Bmatrix} \;\equiv\; \begin{bmatrix} - & \hat{\mathbf{b}}_{1_i} & - \\ - & \hat{\mathbf{b}}_{2_i} & - \end{bmatrix} \cdot \begin{Bmatrix} | \\ \hat{\mathbf{d}}_i \\ | \end{Bmatrix} \tag{109}$$

Either one or two of these residuals can be imposed, as dictated by the physical boundary condition. A clamped edge or a single symmetry plane edge would have only the $\mathcal{R}_i^{m_1}$ replaced with $\mathcal{R}_i^{d_1}$. A double symmetry plane edge would have both residuals replaced, thus completely specifying the $\hat{\mathbf{d}}_i$ vector at that node.

IX. Newton Solution

All the discrete residuals are driven to zero by a standard Newton method. For the pure structural shell problem the linear Newton system is

$$\left[\frac{\partial \vec{\mathcal{R}}_i}{\partial \vec{v}_i} \right] \left\{ \delta \vec{v}_i \right\} = - \left\{ \vec{\mathcal{R}}_i \right\} \tag{110}$$

where $\vec{\mathcal{R}} = (\mathcal{R}^{f_1}, \mathcal{R}^{f_2}, \mathcal{R}^{f_n}, \mathcal{R}^{m_1}, \mathcal{R}^{m_2})$ and $\vec{v} = (r_1, r_2, r_n, d_1, d_2)$ are the projected residuals and variables. The Jacobian is computed exactly from the current solution at each iteration. It is sparse and well conditioned due to the Poisson-type form of all the equations, and hence is well suited for iterative solution, especially for large problems. The usual Newton update is then performed, possibly with an underrelaxation factor ω.

$$\vec{v}_i \;\leftarrow\; \vec{v}_i \,+\, \omega\, \delta \vec{v}_i \tag{111}$$

Provided there are no structural instabilities (e.g. buckling) present, $\omega = 1$ can be set and convergence is typically rapid. For strong geometrically nonlinear problems with large deformations, $\omega < 1$ is typically needed initially, set either via line search, or heuristically such that the position changes do not exceed some specified fraction of the body dimensions, and that the director changes do not exceed some modest angle.

X. Example Test Cases

A. Beam in pure bending

Many problems in nonlinear aeroelasticity feature large deformations. A popular test case for such problems is a uniform cantilevered plate beam of length L, subjected to a bending moment load $m_{x_{\mathrm{BC}}}$ at its tip edge, as shown in Figure 10. With $\nu = 0$, the exact solution is $m_{11} = -m_{x_{\mathrm{BC}}}$ everywhere (1 is the lengthwise direction), with all other stress resultants being zero. The deformed beam shape is a circular arc with curvature $\kappa_{11} = m_{11}/D_{11}$, so that the particular load $m_{x_{\mathrm{BC}}} = 2\pi D_{11}/L$ deforms the beam into a circle.

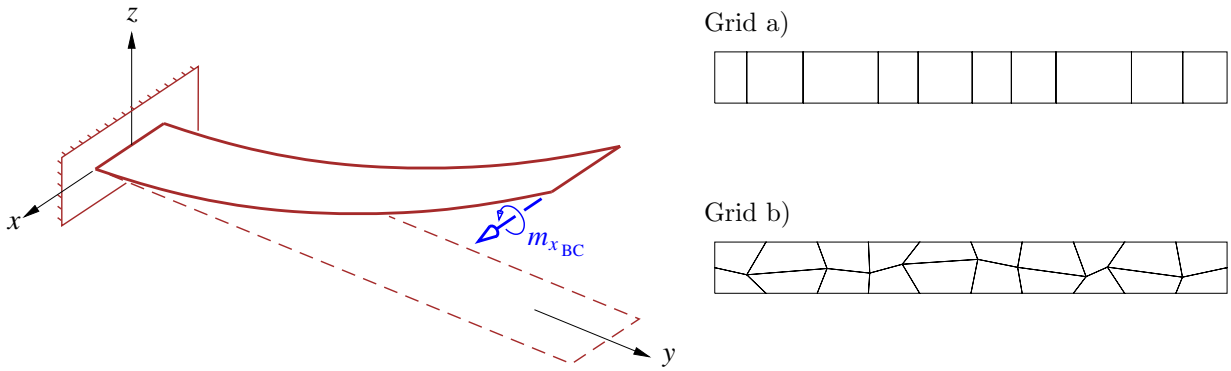

Figure 10. Plate beam deformed into an arc by an applied tip bending moment.

Figure 11 shows the computed shapes with grid a) in Figure 10, for standard bilinear interpolation, and for the HSM scheme with spherical interpolation of $\hat{\mathbf{d}}$ and projected basis vectors $\mathbf{a}_\alpha$ given by (21). The HSM formulation produces the exact solution for this case for any number of elements. The shell thickness ratio is $t/L = 0.025$, although this is not relevant for this pure-bending problem since the in-surface membrane stresses are zero.

For more general cases and irregular grids the HSM solution is not exact, but it does greatly improve accuracy for bending-dominated cases. Figure 12 shows the solution error versus the average element size

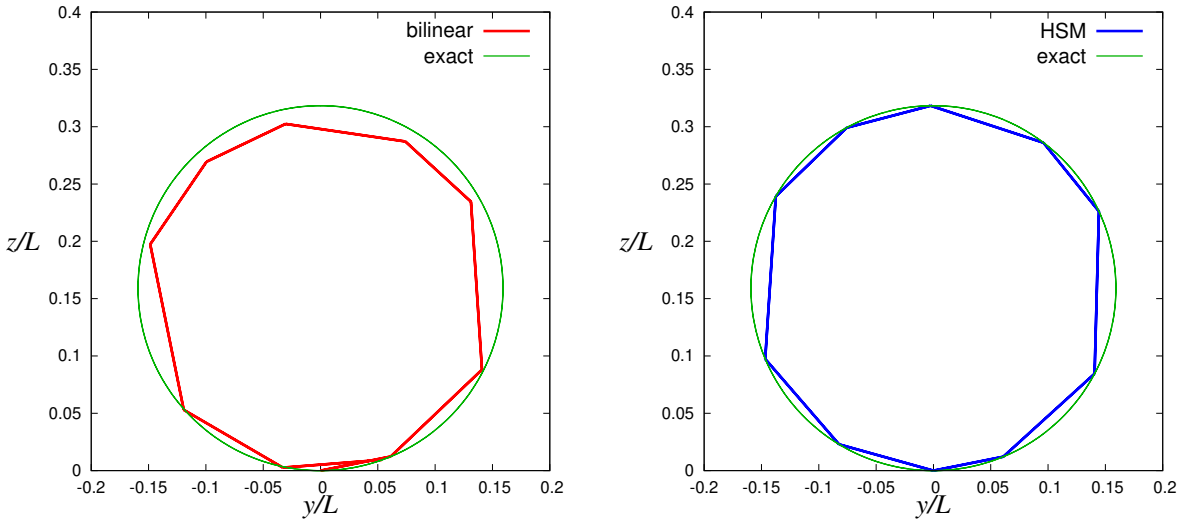

Figure 11. Side view of plate beam with 10 rectangular elements deformed into circle, computed with standard and HSM modeling options, as described in the text.

for the circular beam, for grid b) shown in Figure 10. Interestingly, correct representation of the C^1 virtual surface in HSM produces 4th-order accuracy for this case, versus the typical 2nd-order accuracy of the standard bilinear method.

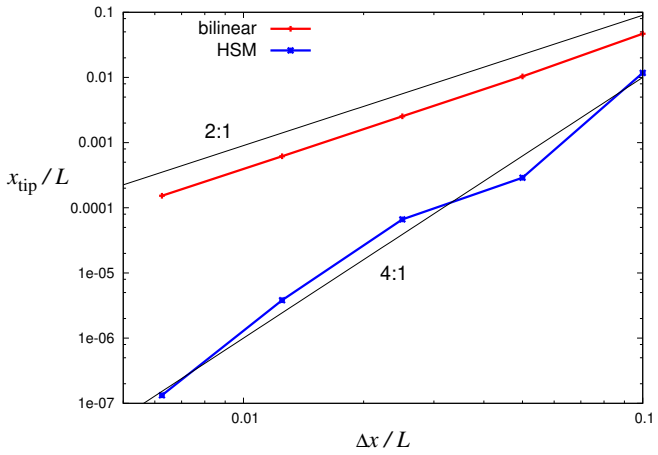

Figure 12. Convergence of tip displacement error for circular beam, using the irregular grid b) shown in Figure 10.

B. Beam buckling

To verify that the nonlinear interaction between membrane loads and curvatures is correctly captured in the present method, the simple beam-buckling case shown in Figure 13 was computed. A zero Poisson ratio is specified to prevent transverse warping of the beam strip of width $w = L/10$, which allows the use of the theoretical buckling load $P_{\text{crit}} = \pi^2 w D_{11}/4L^2$ as the reference solution. The actual buckling load P is implemented by imposing on the tip edge a combined a force/length $f_{y_{\text{BC}}} = -P/w$ together with a moment/length $m_{x_{\text{BC}}} = 0.002P$ to give a small eccentricity. As expected, the tip deflections increase very rapidly as P approaches P_{crit}, as shown in Figure 13 on the right.

Figure 14 shows a zoom-in of the tip deflections near $P/P_{\text{crit}} = 1$, and the grid convergence for the largest computed load $P/P_{\text{crit}} = 0.995$. The usual 2nd-order accuracy of conventional shell methods is observed, but the absolute error of the HSM formulation is more than an order of magnitude smaller, and even more so for the coarsest grid. This accuracy is attributable mainly to the higher-order position vector definition (31), which models the curvature of an individual element. This therefore gives a higher-order representation of

the interaction between the curvature and axial stress, which is the primary column-buckling mechanism.

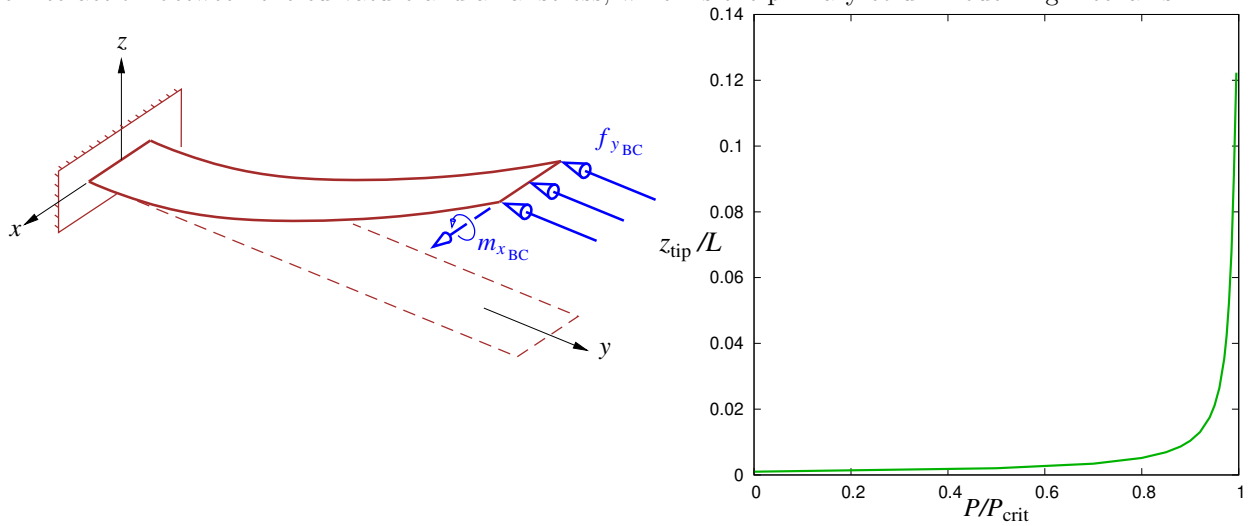

Figure 13. Plate beam is subjected to a buckling load P and a small tip moment to simulate load eccentricity. Computed deflection versus P is shown on the right.

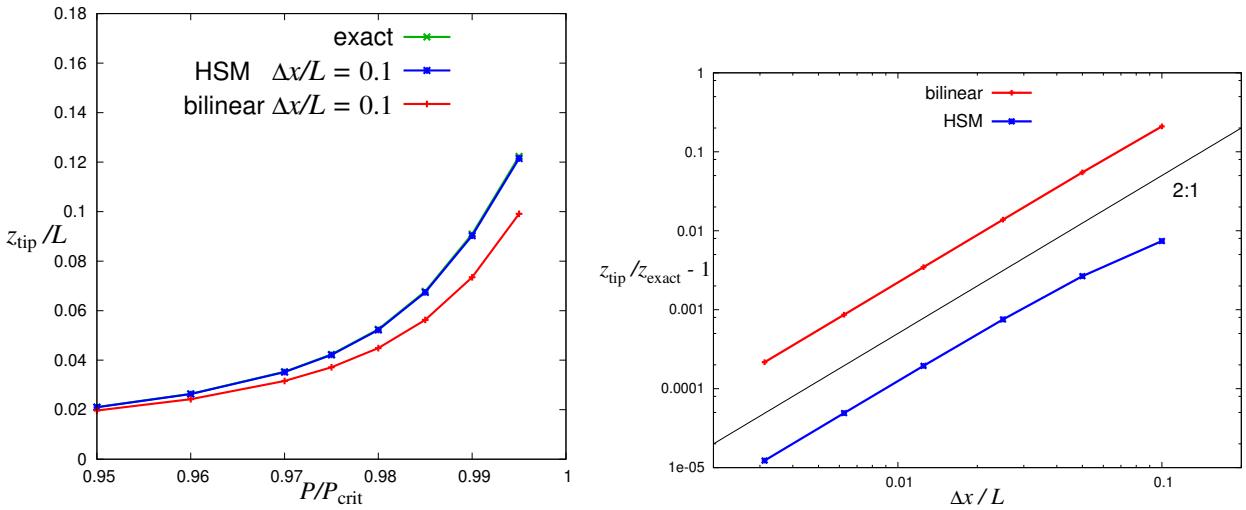

Figure 14. Errors in computed tip deflection for $P/P_{crit} = 0.995$ versus element size.

C. Tube beam with incipient shell buckling

To verify that various types of shell buckling and wrinkling can be predicted, the end-loaded hollow tube beam case shown in Figure 15 was computed for a range of grids. The tube radius and wall-thickness ratios are $R/L = 0.1$, $h/R = 0.1$. A simple pinned support boundary condition was specified at the anchor end on the $y = 0$ plane. A vertical force/length $f_{z_{BC}}$ was imposed on the tube edge at the free end, giving a total vertical loading force $F = 2\pi R f_{z_{BC}}$.

As expected, this case exhibits local buckling for a sufficiently large tip load F. In the solution it is manifested by the failure of the Newton iteration to converge, due to the non-existence of a solution for a tip load which exceeds the maximum supportable buckling load F_{max}. Figure 16 shows the shell axial and circumferential curvatures for a solution at the onset of buckling computed on the finest grid. A tube-ovalization buckling mode is evident, and features an inward "dent" with negative κ_{11} on the upper surface roughly 1.5 diameters out from the anchored end. Also visible is another conventional column-type buckling mode characterized by an outward bend with positive κ_{11} immediately adjacent to the anchor end. Figure 15

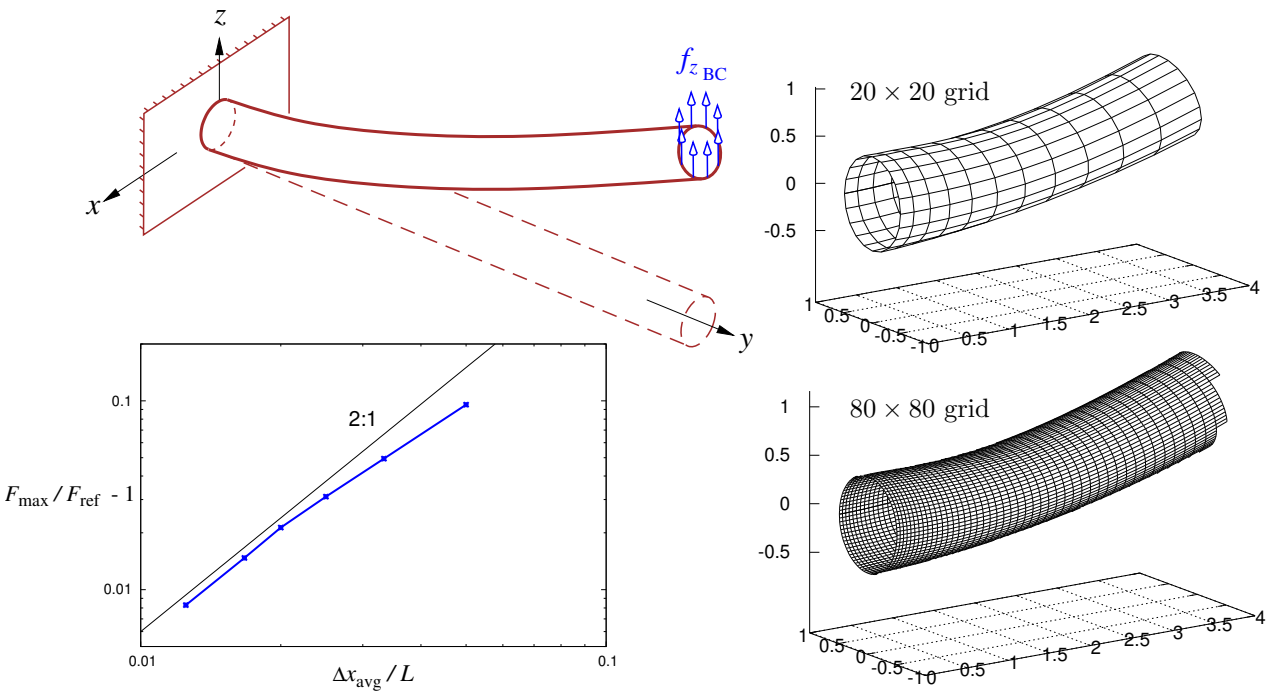

Figure 15. Tube beam is subjected to a vertical load on its free edge to investigate curved-shell buckling and wrinkling. Wall-anchor ends of coarsest and finest grids used are shown at incipient-buckling solution. Grid convergence of total buckling-onset tip load shown on bottom left.

on bottom left shows the grid convergence of the buckling load relative to the reference F_{ref}, which is obtained by Richardson extrapolation from the three finest-grid $F_{\max}$ values.

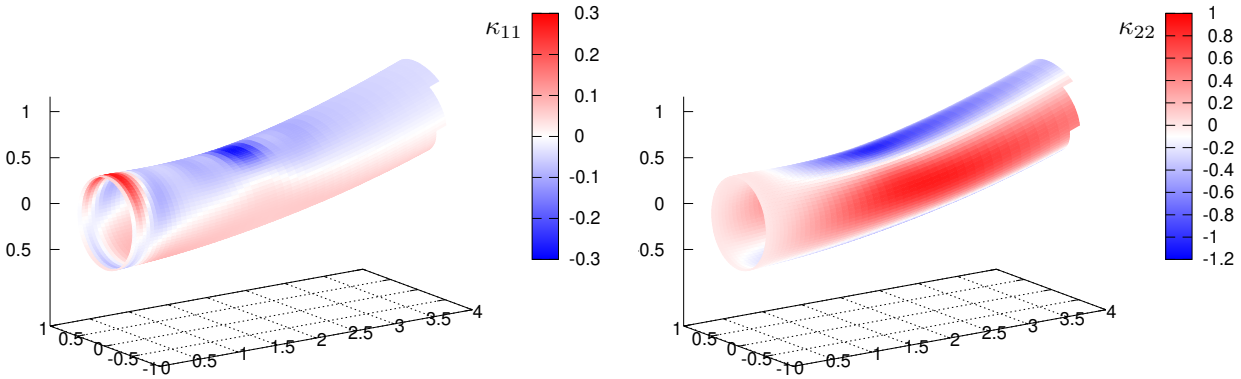

Figure 16. Distributions of bending curvature strains κ_{11} and κ_{22} in the axial and circumferential directions, respectively, computed on the 80×80 grid.

D. Wing shell beam

Figure 17 shows a wing-like closed shell beam, with vertical loading taken from 2D airfoil surface pressures. Figure 18 is the same beam with the loading increased by a factor of 1.5×. The tip deflection is more than doubled, due to localized buckling of the shell near the root, shown in Figure 19. This again shows that the present nonlinear HSM formulation is able to capture structural instabilities like buckling in realistic structural shapes.

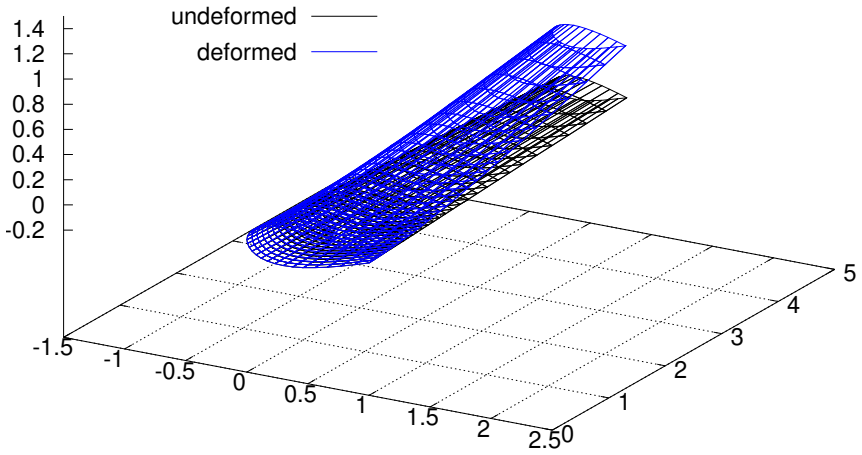

Figure 17. Wing-like shell beam under deformation from 2D aero loads.

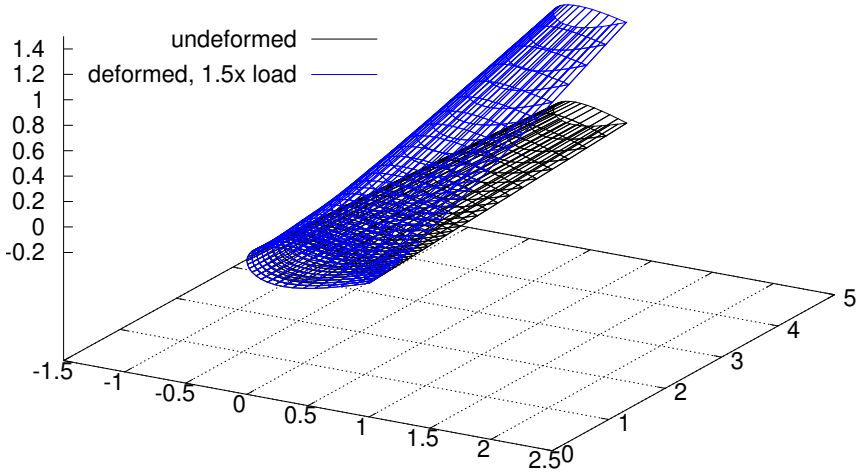

Figure 18. Same as in Figure 17, but with applied loads increased by factor of $1.5\times$.

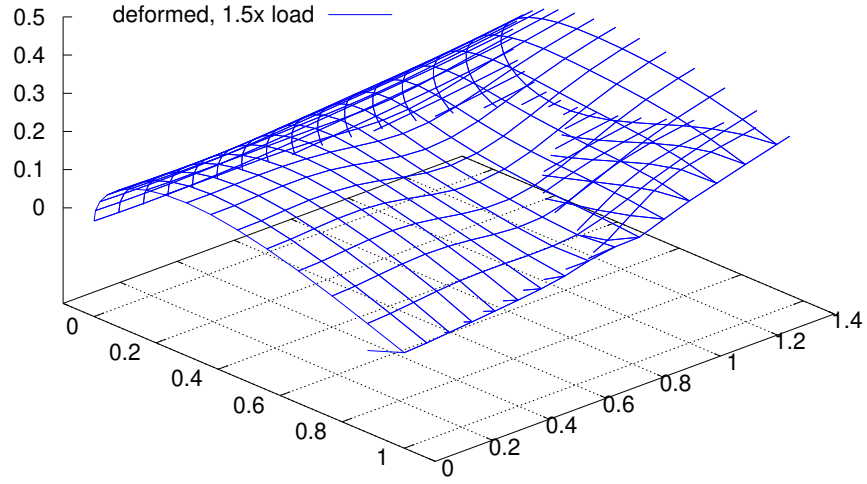

Figure 19. Detail of the case in Figure 18, showing shell buckling near the wing root.

XI. Conclusions

This paper presented the HSM finite element formulation, which introduces higher-order treatments into existing nonlinear shell methods to more accurately represent shells with large element curvatures. This makes the method particularly attractive for intermediate-fidelity nonlinear aeroelastic problems, where relatively coarse grids are desirable to achieve computational economy. Example solutions demonstrated the ability of HSM to achieve improved accuracy over conventional methods, especially for bending-dominated problems with large deformations and buckling.

Acknowledgements

This work was funded by the CAPS project, AFRL Contract FA8050-14-C-2472: "CAPS: Computational Aircraft Prototype Syntheses"; Dean Bryson is the Technical Monitor.

References

[1]Ahmad, S., Irons, B., and Zienkewicz, O., "Analysis Of Thick And Thin Shell Structures By Curved Finite Elements," *Int. J. Num. Meth. Eng.*, Vol. 2, 1970, pp. 419–451.

[2]Sanders, J.L., J., "Nonlinear Theories for Thin Shells," Technical Report 10, Division of Engineering and Applied Physics, Harvard University, Feb 1961.

[3]Dvorkin, E. and Bathe, K., "A continuum mechanics based fournode shell element for general nonlinear analysis," *Engineering Computations*, Vol. 1, No. 1, 1984, pp. 77–88.

[4]Simo, J. and Fox, D., "On a Stress Resultant Geometrically Exact Shell Model. Part I: Formulation and Optimal Parametrization," *Computer Meth. in Appl. Mechanics and Eng.*, Vol. 72, 1989, pp. 267–304.

[5]Simo, J., Fox, D., and Rifai, M., "On a Stress Resultant Geometrically Exact Shell Model. Part III: Computational Aspects of the Nonlinear Theory," *Computer Meth. in Appl. Mechanics and Eng.*, Vol. 79, 1990, pp. 21–70.

[6]Lee, Y., Lee, P., and Bathe, K., "The MITC3+ Shell Element and Its Performance," *Computers and Structures*, Vol. 138, 2014, pp. 12–38.

[7]Talamini, B. and Radovitzky, R., "A discontinuous Galerkin method for nonlinear shear-flexible shells," *Comput. Methods Appl. Mech. Engrg.*, Vol. 303, 2016, pp. 128–162.

[8]Simo, J., Fox, D., and Rifai, M., "On a Stress Resultant Geometrically Exact Shell Model. Part II: The Linear Theory; Computational Aspects," *Computer Meth. in Appl. Mechanics and Eng.*, Vol. 73, 1989, pp. 53–92.